

Original Article

Cite this article: Torgersen E, Gabrielsen RH, Ganerød M, van der Lelij R, Schönenberger J, Nystuen JP, and Brask S. Repeated brittle reactivations of a pre-existing plastic shear zone: combined K–Ar and ^{40}Ar – ^{39}Ar geochronology of the long-lived (>700 Ma) Himdalen–Ørje Deformation Zone, SE Norway. *Geological Magazine* <https://doi.org/10.1017/S0016756822000966>

Received: 28 January 2022

Revised: 29 August 2022

Accepted: 30 August 2022

Keywords:


fault activity; reactivation; fault gouge geochronology; pseudotachylite; Oslo Rift

Author for correspondence:

Espen Torgersen,

Email: espen.torgersen@ngu.no

Repeated brittle reactivations of a pre-existing plastic shear zone: combined K–Ar and ^{40}Ar – ^{39}Ar geochronology of the long-lived (>700 Ma) Himdalen–Ørje Deformation Zone, SE Norway

Espen Torgersen^{1,2} , Roy H. Gabrielsen³, Morgan Ganerød¹, Roelant van der Lelij¹, Jasmin Schönenberger¹, Johan Petter Nystuen³ and Sofie Brask³

¹Geological Survey of Norway – NGU, Trondheim, Norway; ²Department of Ocean Operations and Civil Engineering-IHB, Norwegian University of Science and Technology – NTNU, Ålesund, Norway and ³Department of Geology, University of Oslo, Oslo, Norway

Abstract

Brittle reactivation of plastic shear zones is frequently observed in geologically old terranes. To better understand such deformation zones, we have studied the >700 Ma long structural history of the Himdalen–Ørje Deformation Zone (HØDZ) in SE Norway by K–Ar and ^{40}Ar – ^{39}Ar geochronology, and structural characterization. Several generations of mylonites make up the ductile part of HØDZ, the Ørje Shear Zone. A ^{40}Ar – ^{39}Ar white mica plateau age of 908.6 ± 7.0 Ma constrains the timing of extensional reactivation of the Ørje mylonite. The mylonite is extensively reworked during brittle deformation events by the Himdalen Fault. ^{40}Ar – ^{39}Ar plateau ages of 375.0 ± 22.7 Ma and 351.7 ± 4.4 Ma from pseudotachylite veins and K–Ar ages of authigenic illite in fault gouge at *c.* 380 Ma are interpreted to date initial brittle deformation, possibly associated with the Variscan orogeny. Major brittle deformation during the Early–Mid Permian Oslo Rift is documented by a ^{40}Ar – ^{39}Ar pseudotachylite plateau age of 294.6 ± 5.2 Ma and a K–Ar fault gouge age of *c.* 270 Ma. The last datable faulting event is constrained by the finest size fraction in three separate gouges at *c.* 200 Ma. The study demonstrates that multiple geologically significant K–Ar ages can be constrained from fault gouges within the same fault core by combining careful field sampling, structural characterization, detailed mineralogy and illite crystallinity analysis. We suggest that initial localization of brittle strain along plastic shear zones is controlled by mechanical anisotropy of parallel-oriented, throughgoing phyllosilicate-rich foliation planes within the mylonitic fabric.

1. Introduction

The term ‘fault’ is derived from French *faute* (opening, gap, failure or flaw) and was first systematically treated as such by Margerie and Heim (1888), later becoming one of the most important elements in geological structural analysis. What makes faults particularly important is that, once formed, they tend to become the loci of permanent weakness in the crust and, whenever favourably oriented with regard to the stress field, may localize significant strain increments (e.g. Holdsworth *et al.* 1997; Naliboff *et al.* 2017). This observation is particularly evident in geologically old terranes where faults may have been reactivated multiple times (e.g. Braathen *et al.* 2004; Redfield & Osmundsen, 2009; Viola *et al.* 2016; Aldega *et al.* 2019; Kemp *et al.* 2019). Some faults record activity that is separated by hundreds of millions of years (e.g. Torgersen *et al.* 2015a; Nordbäck *et al.* 2022), which demonstrates that faults can control crustal strengths over very long timescales even though they are inactive at subcritical stress conditions for most of the time. This long-lived strength reduction is partly a consequence of the loss of cohesion along faults (Sibson, 1985), but more significantly due to the anomalously low friction coefficients of clay minerals and phyllosilicates that commonly make up the fault cores (e.g. Haines *et al.* 2014; Colletini *et al.* 2019). Combined mechanical comminution and fluid–rock interactions cause the formation of interconnected clay/phyllosilicate-decorated slip surfaces or foliation planes, which appears to be the primary process causing progressive strain weakening in large fault zones (Colletini *et al.* 2009; Haines *et al.* 2013; Torgersen & Viola, 2014). Whereas this process may readily explain why pre-existing clay/phyllosilicate-rich faults are primed for repeated brittle reactivations, it does not fully account for how brittle faults can localize into and exploit pre-existing plastic shear zones. This type of structural superposition is observed along many major deformation zones (e.g. Braathen *et al.* 2004; Ferreira *et al.* 2008; Salomon *et al.* 2015; Scheiber *et al.* 2015; Gabrielsen *et al.* 2019), and offshore seismic studies show that basement-hosted plastic shear zones control fault localization and magnitude in the unconformably overlying sedimentary rocks (e.g. Phillips *et al.* 2018; Osagiede *et al.* 2020). Pre-existing plastic

© The Author(s), 2022. Published by Cambridge University Press. This is an Open Access article, distributed under the terms of the Creative Commons Attribution licence (<http://creativecommons.org/licenses/by/4.0/>), which permits unrestricted re-use, distribution and reproduction, provided the original article is properly cited.



shear zones may even impact on the entire architecture and geometry of rifted margins (e.g. Morley *et al.* 2004; Fossen *et al.* 2017; Osmundsen & Péron-Pinvidic, 2018; Kalani *et al.* 2020; Osmundsen *et al.* 2021).

The superposition of brittle deformation on plastic shear zones is frequently observed along major low-angle detachment zones (e.g. Norton, 1986; Andersen & Jamtveit, 1990; Fossen, 1992; Osmundsen *et al.* 2006). These often demonstrate a continuum of deformation rocks, reflecting the progressive development during semi-continuous exhumation through the brittle–plastic transition (Davis *et al.* 2002; Braathen *et al.* 2004). In such a situation, brittle deformation is closely spaced in time with visco-plastic deformation and it is suggested that the transition between the two is controlled by ingress of fluids and reaction-driven mineralogical (and rheological) changes (Selverstone *et al.* 2012). As such, one may question whether a progressive exhumation is always required for brittle deformation to localize along plastic shear zones, or if other mechanisms may lead to brittle reactivation that is kinematically and temporally distant.

If one only considers the frictional properties of plastic shear zones, it appears counter-intuitive that brittle faults should localize along such structures because the fine-grained, dynamically recrystallized mylonites that commonly make up the shear zones should have at least as high a frictional coefficient as the surrounding wall rocks. Mechanisms such as post-tectonic alteration-weakening (Backeberg *et al.* 2016), strength anisotropy associated with the mylonitic/phyllonitic fabric (e.g. Crider, 2015; Bolognesi & Bistacchi, 2016; Samsu *et al.* 2021) and stiffness contrasts combined with grain-size reduction and mineral alteration (e.g. Jefferies *et al.* 2006) have been proposed to explain this behaviour.

To improve the understanding of how brittle deformation may repeatedly localize along existing plastic shear zones, we have studied the Himdalen Fault in southeast Norway (Fig. 1), which is formally defined and described for the first time in this paper. The fault is associated with a strong topographic lineament that parallels the surrounding mylonitic fabric of the Ørje Shear Zone, a Meso- to Neoproterozoic orogen-scale high-strain zone associated with the development of the Sveconorwegian orogeny in southern Norway and Sweden (Fig. 1; Skjerna, 1972; Viola *et al.* 2011; Bingen *et al.* 2021). Collectively, the herein termed Himdalen–Ørje Deformation Zone (HØDZ) is defined by a series of deformational products ranging from mylonite and cataclaste to pseudotachylite, breccia and gouge following the combined extent of the Himdalen Fault and the Ørje Shear Zone. The mylonitic component has been attributed to Sveconorwegian top-to-the-SE contractional deformation and subsequent post-orogenic top-to-the-W extensional reactivation (Viola *et al.* 2011). Apart from these structural inferences, no radiometric ages are yet available for any of these deformational products, which prevents us from organizing the deformation zone into a correct time frame and understanding the superposition of brittle on visco-plastic deformation products.

In this paper we aim to constrain the structural history of the HØDZ by combining mapping of its structural architecture and deformation products with K–Ar fault gouge dating and ⁴⁰Ar–³⁹Ar geochronology of pseudotachylite veins, and of K-feldspar and white mica in the mylonites. We focus on constraining the timing of brittle reactivation along the Himdalen Fault, which may potentially be hundreds of millions of years younger than the assumed Meso- to Neoproterozoic mylonitic Ørje Shear Zone. The results provide new insights into the structural evolution of a long-lived plastic-to-brittle deformation zone and the

mechanisms that control repeated structural reactivations. The study also demonstrates the use and challenges of illite crystallinity in interpreting multi-reactivated fault gouges. The new ages provide important novel constraints on the timing of the tectonic development of southern Norway and Sweden, as well as the offshore Skagerrak graben and potentially the Sorgenfrei–Tornquist zone.

2. Geological setting

The HØDZ is situated in SE Norway within the Sveconorwegian domain of the Precambrian basement in southern Norway and Sweden (Gaal & Gorbatschev, 1987; Andersen, 2005; Bingen *et al.* 2008b, 2021; Slagstad *et al.* 2013; Fig. 1). The Sveconorwegian orogeny took place in the late Mesoproterozoic to early Neoproterozoic during a hot, long-duration continental collision between proto-Baltica and another plate, possibly Amazonia (Bingen *et al.* 2021). The rocks within the Sveconorwegian domain are affected by numerous generally NNW–SSE-striking crustal-scale shear zones separating different lithotectonic units, previously termed sectors, segments (Berthelsen, 1980; Starmer, 1996), terranes (e.g. Bingen *et al.* 2008b; Viola *et al.* 2011) and blocks (Andersen, 2005). The Scandinavian Deformation Front / Protogene Zone, the Mylonite Zone and the Dalsland Boundary Thrust / Göta Älv Shear Zone / Lerdal Shear Zone / Ørje Shear Zone (Berthelsen, 1980; Park *et al.* 1991; Stephens *et al.* 1996) are the most conspicuous shear zones east of the Oslo Rift, whereas the Kristiansand–Porsgrunn and Saggrenda–Sokna Shear Zones separate the Bamble and Kongsberg Lithotectonic Units, respectively, from the Telemarkia Lithotectonic Unit to the west (Mulch *et al.* 2005; Scheiber *et al.* 2015; Fig. 1a). Each block is, however, further dissected by internal high-strain zones (mylonites sometimes overprinted by cataclastes) branching out from the main shear zones (e.g. Park *et al.* 1991; Andersen, 2005; Bingen & Viola, 2018). The peak metamorphism in the Idefjorden Lithotectonic Unit east of the Oslofjord is dated to 990 Ma (eclogite facies; Munz *et al.* 1994; Möller *et al.* 2015; Pinán-Llamas *et al.* 2015; Möller & Andersson, 2018) and between 1140 and 1075 Ma in the Kongsberg and Bamble Lithotectonic Units to the west (granulite facies; Andersen & Grorud, 1998; Bingen *et al.* 2001, 2008a; Bingen & Viola, 2018).

Dedicated chronological data for the timing of shear zones in the Sveconorwegian domain are generally less common and precise. One sample taken close to the Göta Älv shear zone gave an age of 974 ± 22 for the outer rim of a zircon (Ahlin *et al.* 2006), and the maximum age of metamorphism (amphibolite facies) is in the range 910–990 Ma (Park *et al.* 1991; Stephens *et al.* 1996 and references therein). U–Pb-dating of titanite in the Mylonite Zone yielded a concordant age of c. 920 Ma, believed to represent the amphibolite metamorphism in the zone (Johansson & Johansson, 1993), whereas Wahlgren & Kähr (1977) dated a post-tectonic lamprophyre dyke crossing the Mylonite Zone to 904 ± 13 Ma (whole-rock K–Ar), representing a minimum age for the visco-plastic deformation there. ⁴⁰Ar–³⁹Ar biotite and white mica ages from greenschist-facies, extension-related shear fabric of the Mylonite Zone range between 922 and 860 Ma (Viola *et al.* 2011), which is a time interval associated with rapid cooling in the whole eastern part of the orogen (Ulmius *et al.* 2018).

West of the Oslofjord, top-to-the-NW contractional displacement associated with the Kristiansand–Porsgrunn Shear Zone is constrained by the Morkheia monzonite suite and the

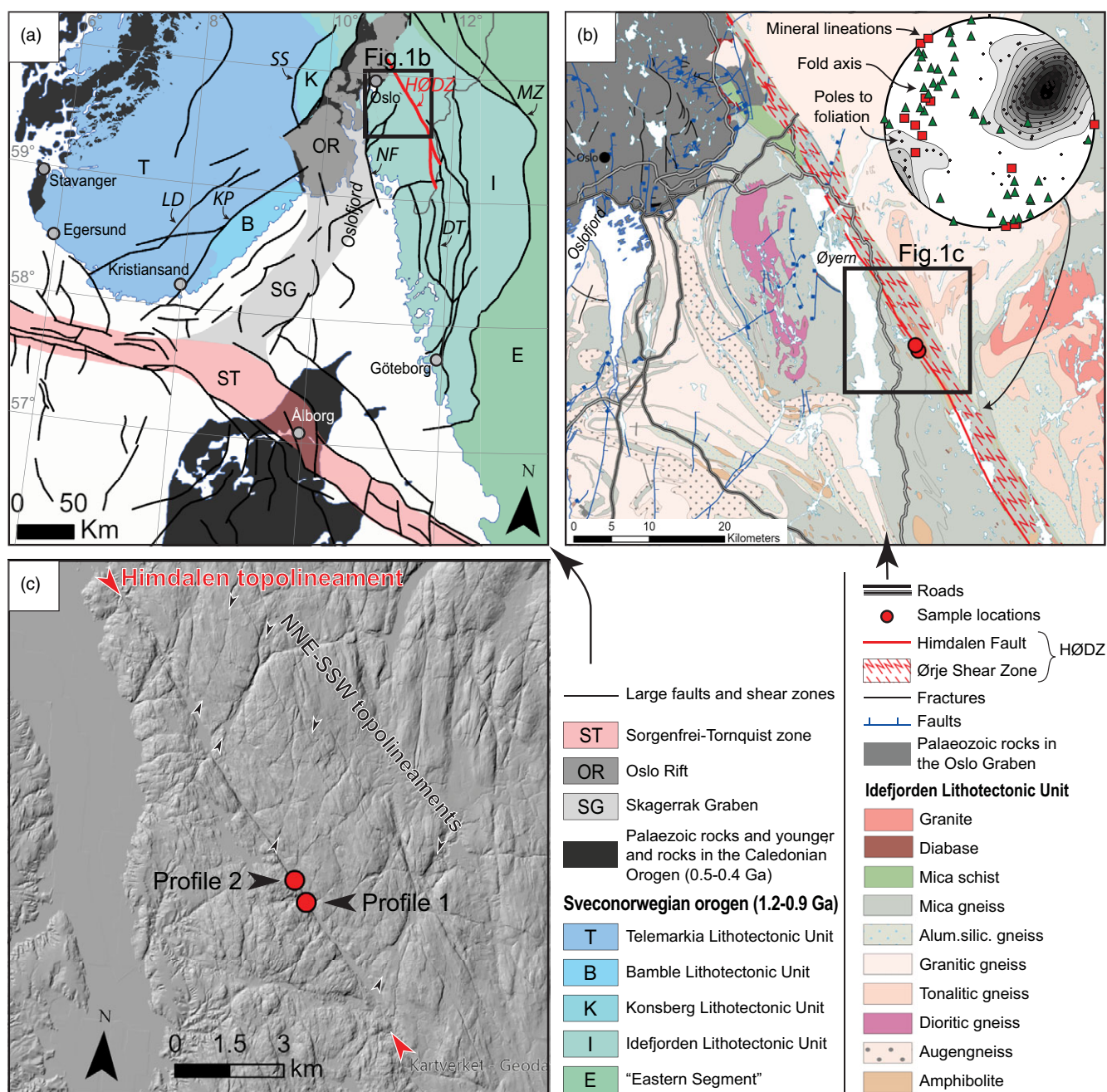


Fig. 1. (Colour online) (a) Geological framework of southwestern Scandinavia. Large structures (in italics): MZ: Mylonite Zone; DT: Dalsland Boundary Thrust / Göta Älv Shear Zone / Lerdal Shear Zone; KP: Kristiansand–Porsgrunn Shear Zone; SS: Saggrenda–Sokna Shear Zone; LD: Listafjorden–Drangedal Fault Complex; NS: Nesodden Fault; HØDZ: Himdalen–Ørje Deformation Zone. (b) Bedrock map (Norges Geologiske Undersøkelse, 2021) of the wider Himdalen region showing the position of the Ørje Shear Zone and the Himdalen Fault. Stereonet plot shows foliation (as poles and contours), fold axis and mineral lineations within the Ørje Shear Zone as presented on published geological maps. (c) Hillshade (light source from NW) showing the Himdalen topolineament and the location of the two structural profiles in Figure 2.

Hovdefjell–Vegårdshei augen gneiss, giving a maximum age between 1132 ± 3 and 1140 ± 13 Ma (Heaman & Smalley, 1994; Bingen & Viola, 2018). In one locality west of Lake Væteren in the Kongsberg Lithotectonic Unit, a post-mylonite lamprophyre dyke was dated to 1033 ± 12 Ma (zircon U–Pb), giving a minimum age for this deformation (Bingen & Viola, 2018). Late overprinting extensional fabrics of the Kristiansand–Porsgrunn Shear Zone are dated to 891 ± 3 Ma by ^{40}Ar – ^{39}Ar geochronology of synkinematic muscovite (Mulch *et al.* 2005).

Some of the N–S- to NNE–SSW-striking master shear zones that constrain the Proterozoic Idefjorden Lithotectonic Unit in

the east and the Kongsberg and Bamble Lithotectonic Units in the west merge with the master faults of the Permian Oslo Graben. These faults display complex structural relations and are characterized by shifting strain, *P–T* conditions and different types of fault rocks including protocataclasite, cataclasite, ultracataclasite and fluid breccia (e.g. Swenson, 1990; Olausen *et al.* 1994; Larsen *et al.* 2008a, b; Torgersen *et al.* 2015b; Gabrielsen *et al.* 2018). Particularly in the northern extension of these faults (north of the northernmost segment of the Oslo Graben) mylonitic rocks are occasionally found in the core of these faults (Gabrielsen *et al.* 2018).

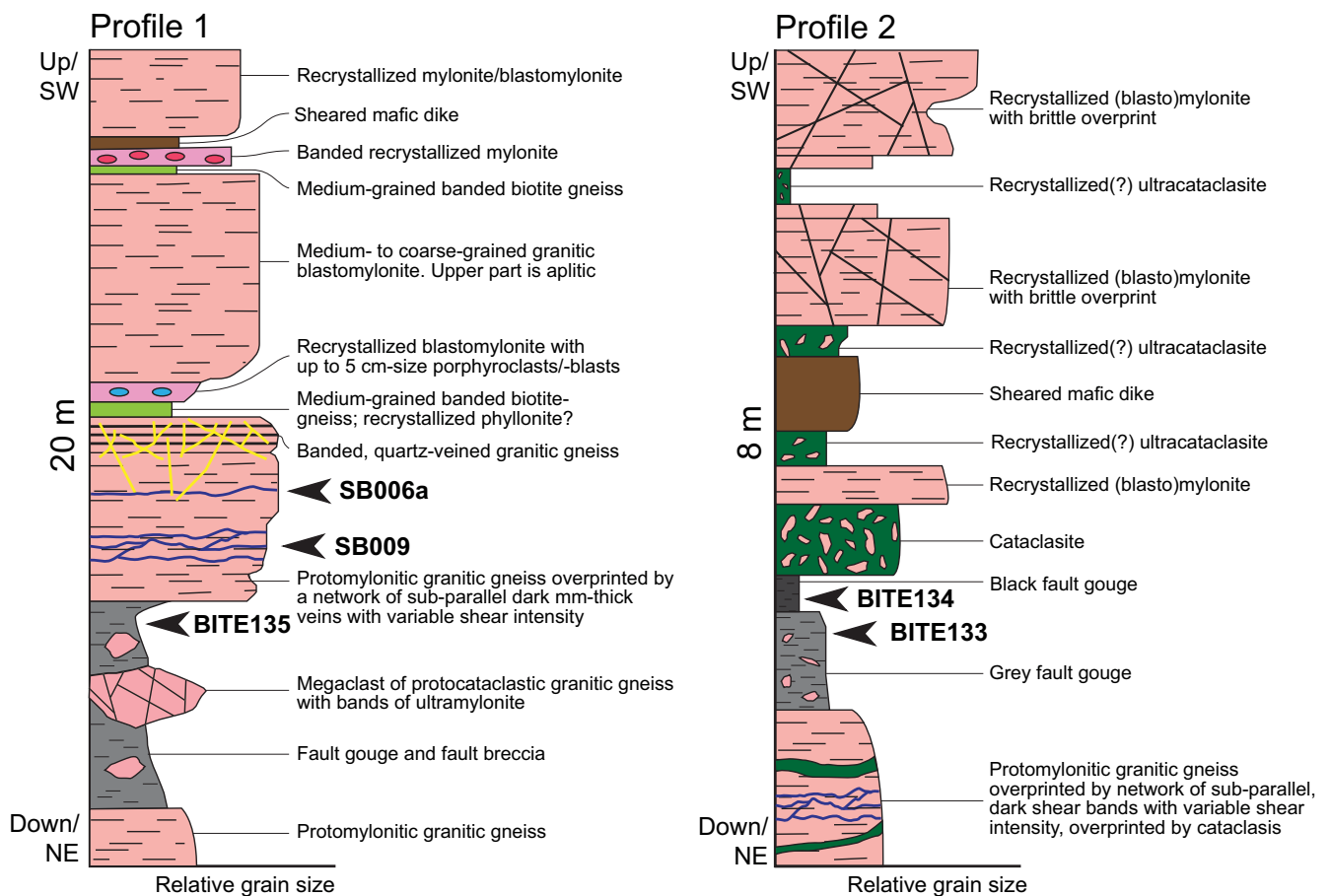


Fig. 2. (Colour online) Structural profiles across the Himdalen–Ørje Deformation Zone with location of geochronological samples. Profile 1 at UTM33N 6633204 293539, profile 2 at UTM33N 6632564 293914.

Several complex and reactivated fault systems in south-central and south Norway are characterized by both visco-plastic and brittle deformation rocks, some of which are composed of fault gouge reaching thicknesses up to tens of metres (e.g. the Sirdal and Listafjorden–Drangedal fault complexes; Gabrielsen *et al.* 2019). Anticipated or documented Permian (or younger) overprint occurs only in some of the shear zone segments. The youngest brittle reactivation in the ‘Great Friction Breccia’ associated with the Saggrenda–Sokna shear zone (Bugge, 1936; Starmer, 1985; Scheiber *et al.* 2015; Bingen & Viola, 2018) has a probable Permian–Triassic age (Larsen *et al.* 2008b; Scheiber *et al.* 2015; Torgersen *et al.* 2015b). This is also the case for the N–S-striking Nesodden fault, which is characterized by multistage ductile deformation with post-Caledonian (Carboniferous–Permian?) brittle fault rocks (e.g. Swensson, 1990; Ganerød *et al.* 2008). Also several other faults north of the Oslo area in the Oslo–Trondheim lineament zone (Gabrielsen & Ramberg, 1979; Gabrielsen & Braathen, 2014), mainly comprising N–S-striking normal faults, display multiphase deformation with visco-plastic (Proterozoic?) and brittle (Carboniferous–post-Permian?) deformation rocks (see Gabrielsen *et al.* 2018 for summary). The presence of often thick accumulation of fault gouge in many of these faults has been used to infer Mesozoic or even Cenozoic reactivation histories (e.g. Gabrielsen *et al.* 2018). Indeed, Mesozoic to recent fault activity has been recorded in the major fault systems of coastal south Norway (Eide *et al.* 1997; Fossen *et al.* 1997; Ksienzyk *et al.*

2016; Fossen *et al.* 2017; Hestnes *et al.* 2022) and in the fault systems in the Kongsberg Lithotectonic Unit (Torgersen *et al.* 2015b).

In summary, age data from mylonitic shear zones in the Sveconorwegian domain display a Sveconorwegian age signature within the timespan *c.* 1050–1033 Ma (Bingen & Viola, 2018). A greenschist facies reactivation of at least some of the shear zones (e.g. the Dalsland Boundary Thrust and the Kristiansand–Porsgrunn Shear Zone) occurred during late stages of the Sveconorwegian orogeny at *c.* 920–890 Ma (Mulch *et al.* 2005). Many of these structures are overprinted by brittle deformation developed concurrently with the border faults of the Permian Oslo Rift or during the Mesozoic subsidence of the Oslo Graben (Torgersen *et al.* 2015b).

2.a. The Himdalen–Ørje Deformation Zone

The Himdalen–Ørje Deformation Zone (HØDZ) is a collective term for the 1–2 km wide NW–SE-trending deformation zone that comprises the Ørje Shear Zone and the Himdalen Fault east of the Oslo Rift (Fig. 1). The Ørje Shear Zone coincides with the eastern margin of the Kongeberg–Marstrand block of Andersen (2005) and is positioned inside the Idefjorden Lithotectonic Unit (Skjerna, 1972; Bingen *et al.* 2001, 2008b). It is a high-strain arch with an average orientation of its mylonitic foliation of 240/45, stretching >100 km from Lillestrøm in the northwest to

Aremark in the south (Fig. 1b). Fold axis and mineral lineation measurements within the Ørje Shear Zone, available in published bedrock maps, plunge overall NW and SE, with a spread towards E–W orientations (Fig. 1b). Viola *et al.* (2011) observed that an early high-grade fabric associated with top-to-the SE compression is partly reworked by later lower-grade (greenschist facies) top-to-the-W extensional shearing.

The Ørje Shear Zone has been traced southwards into the Grann zone (Hageskov, 1980), which is a local equivalent to the Dalsland boundary thrust (Berthelsen, 1980; Gorbatshev, 1988; Park *et al.* 1991) and is accordingly regarded as a part of the Dalsland boundary thrust and the Lerdal zone system (Berthelsen, 1980; Park *et al.* 1991). The latter is described as an imbricate stack of shear zones dipping 20–40° to the W and with a top-to-the-E displacement (Park *et al.* 1991). The eastern flank of the imbricate stack records extensional reactivation at lower-grade conditions and top-to-the-W sense of shear.

The Himdalen Fault is a previously unnamed section within the Ørje Shear Zone ('Ørje crush zone' of Skjerna, 1972) defined by a clear brittle overprint and a distinct topographic expression (Fig. 1c). Skjerna (1972) states that 'crush zone' is an appropriate characterization 'because real mylonites are uncommon', although mylonite gneiss, blastomylonite, phyllonite and 'hartschiefer' (ultramylonite) have previously been described along the continuation of the zone (Quensel, 1916; Skjerna, 1972). Our mapping indicates that the Himdalen section contains a plethora of mylonite gneisses overprinted by a sequence of brittle deformation products.

3. Architecture of the Himdalen–Ørje Deformation Zone

In the Himdalen study area, the HØDZ is characterized by a several tens of metres thick zone of deformation rocks including blastomylonite, mylonite, cataclasite and fault breccia and gouge. The zone varies in thickness, deformation style and intensity along its strike. The Himdalen Fault is traceable in the landscape as a NW–SE-striking topographic lineament (Fig. 1c) with a relief in the order of 100 m, that approximately follows the southwestern, hanging-wall margin of the Ørje Shear Zone (avg. mylonitic foliation dipdir/dip: 240/45). The Himdalen Fault dips moderately to the SW (225/45) and has sharp undulating contacts with the surrounding highly fractured to cataclastic granitic mylonites. It interferes with a NNE–SSW-striking pattern of topographic lineaments, some of which occur only on its NE margin, possibly representing fault splays (Fig. 1c). Normal, top-to-the-SW kinematic is inferred based on the presence of steep second-order fractures (230/70) interpreted as synthetic Riedel shears (Fig. 4f further below).

The architecture of the HØDZ is here presented in two structural profiles along the SW slope of the Himdalen lineament (Figs 1c, 2).

Profile 1 displays a more than 20 m thick zone dominated by rock lenses of granitic gneiss of moderate to intense deformation (Fig. 3a). The lowest part of the exposure comprises a protomylonitic granitic gneiss that is intensely overprinted by brittle deformation, and structurally overlain and cut by fault gouge and unconsolidated breccia. The gouge and breccia are partly covered by and intermingled with coarse to fine erosional deposits; however, 'windows' in the unconsolidated deposits display sheared and intensely fractured granitic gneiss verging into open (unconsolidated) breccia and fault gouge. These windows are interpreted as parts of the fault footwall and likely represent large fragments or lenses embedded in the fault gouge/unconsolidated breccia.

A sharp border separates the fault gouge / unconsolidated breccia from a 1.5 m thick moderately to strongly sheared gneiss sequence above it (Fig. 3a–c). The lowermost 80 cm of the gneiss sequence, a protomylonitic gneiss with lens-shaped protoclasts, is separated by mm-thick sub-horizontal dark shear lozenge-shaped rock fragments. The rock is cross-cut by dark planar to irregular veinlets which are interpreted as pseudotachylite and/or ultracataclasite veins (Fig. 3c). This rock grades into a banded granitic gneiss overprinted by arrays of a 0.1–1 cm thick grey chequerboard pattern of quartz veins, defined by high-angle veins and sills.

A c. 30 cm thick band of biotite-rich dark gneiss and augen gneiss separates the granitic protomylonite sequence from another less intensely deformed granitic unit above it. The biotite-gneiss/augen-gneiss zone is interpreted as a recrystallized high-strain zone that possibly consisted of a phyllonite–blastomylonite sequence. It is structurally overlain by a more than 3 m thick unit of medium- to coarse-grained granitic blastomylonite that encompasses an aplitic, massive unit, which may represent a sheared (?syntectonic) granitic sill. The granitic blastomylonite also contains a 30 cm thick sequence of medium-grained biotite gneiss, recrystallized blastomylonite and a strongly sheared basic rock. The latter presumably is a sheared basic sill.

Profile 2 is situated c. 500 m NW of profile 1 (Figs. 2, 4). The profile has much in common with profile 1, albeit with differences in thickness of the units, probably due to the fault architecture of the master fault, which is characterized by lozenge-shaped rock bodies that have restricted along-strike continuity.

In profile 2, the deepest exposed unit is a protomylonitic granitic gneiss with dark mm-thick zones of ultramylonite or ultracataclasite overprinted by a network of open brittle fractures representing either a lens of deformed country rock or the footwall (Fig. 4a, b). The first interpretation is considered the most likely. In places, the lowermost unit comprises amphibolitic mylonite with microscale asymmetric porphyroclasts (Fig. 4c, d). The protomylonitic granitic gneiss is overlain by a zone of fault gouge / unconsolidated breccia similar to that seen in the lower part of profile 1.

The fault gouge / unconsolidated breccia comprises various subunits described in detail in Section 4.a, below, and has a sharp contact to a c. 0.5 m thick cataclasite above it. The contact is characterized by high-angle fractures interpreted as synthetic riedel shears indicating top-to-the-SW normal displacement (Fig. 4e, f). Profile 2 also contains a deformed dark rock (probably a sheared basic sill) surrounded by recrystallized fine-grained cataclasite/ultracataclasite. The available part of profile 2 is topped by a c. 2 m thick unit of recrystallized protomylonite/blastomylonite.

3.a. Description of geochronological samples

Three fault gouge samples were collected from the two profiles for K–Ar fault gouge geochronology (Figs 1c, 2). At profile 2, a >30 cm thick fault core with two distinct fault gouges is observed (Figs 4e, f, 5a). The lower gouge (BITE133) is at least 15 cm thick, has a sandy to clayey texture and contains abundant angular clasts of the underlying protomylonitic granitic gneiss. The upper gouge (BITE134) is 5–10 cm thick, black to dark grey, without significant visible rock fragments, and with a strongly clayey texture (high plasticity). The contact between the two gouges is sharp and irregular (Fig. 5a). Samples BITE133 and BITE134 were collected c. 10 cm structurally from each other.

Sample BITE135 comes from profile 1 c. 500 m along-strike to the SE from profile 2 (Figs 1c, 2, 3a). The sample is a varicoloured (grey–green to black–brownish), clay-rich sandy gouge that makes

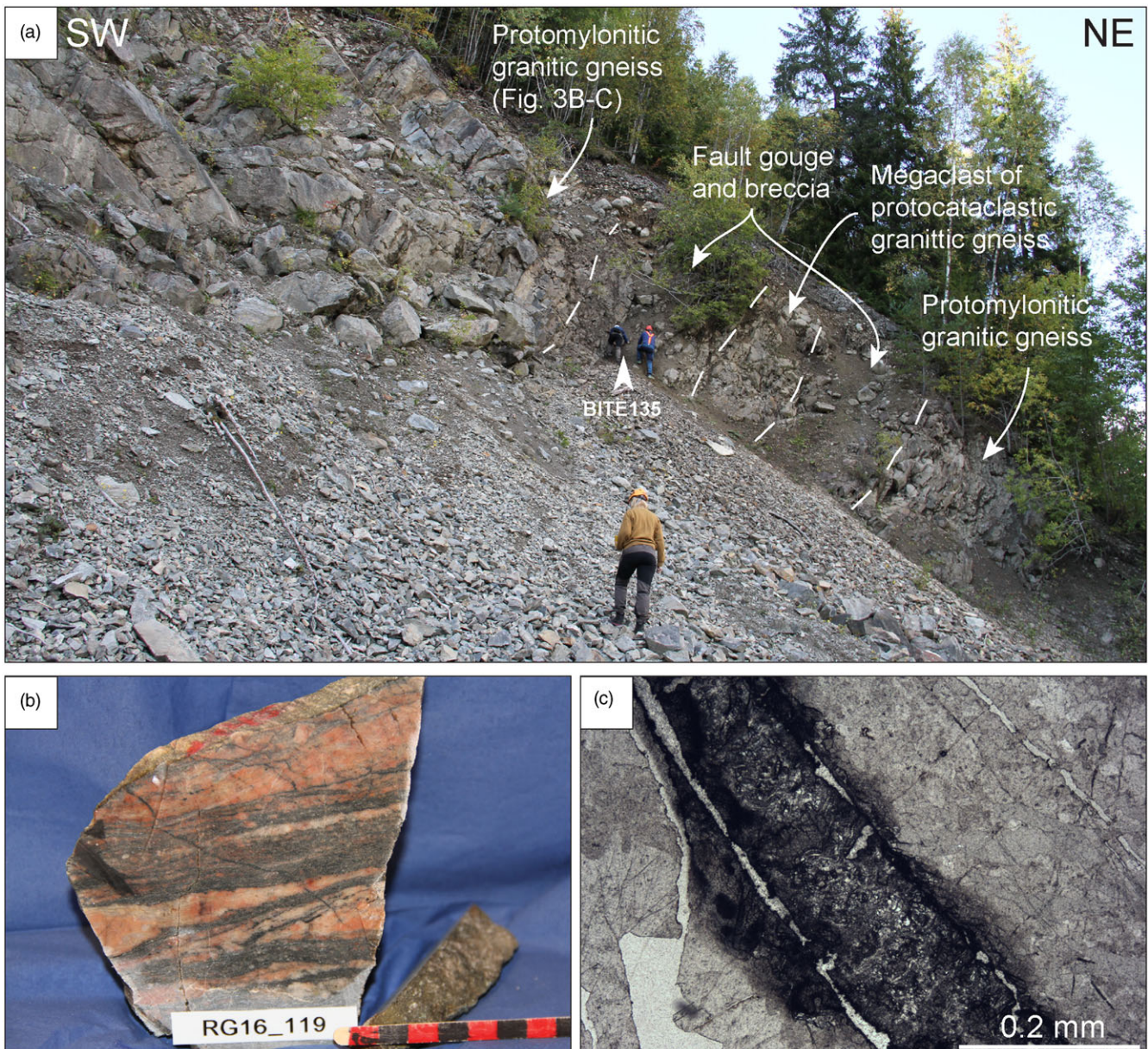


Fig. 3. (Colour online) Field, hand-specimen and thin-section photos of typical deformation rocks in the HØDZ at profile 1, UTM33N 6633204 293539. (a) Overview photograph of the lower portion of profile 1. (b, c) Ultramylonitic band in granitic mylonite with thin cross-cutting pseudotachylite veins (sample RG16-119A2). (c) Photomicrograph (plane polarized) of one of the thin veins in (b), possibly representing a recrystallized pseudotachylite.

up a c. 10 cm thick fault core. The core is situated along the hanging-wall side of a 1.5–2 m wide fault zone composed of highly fractured to brecciated mylonite. The sandy character of the fault gouge is comparable to the grey gouge sampled by BITE133 in profile 2.

Two samples (SB006A and SB009) of protomylonite with strong brittle overprint were selected for ^{40}Ar – ^{39}Ar geochronology to date the timing for both visco-plastic and brittle deformation. The samples were collected from profile 1 in a protomylonitic interval immediately above the fault gouge sampled by BITE135 (Figs 1, 2, 5b, c). Both are protomylonitic granitic gneiss with faint (SB009) to moderately (SB006A) developed mylonitic foliation and numerous cross-cutting dark veins (Fig. 5b, c). In SB009, the veins are distinctly black with few protoclasts and sharp, curvilinear boundaries, whereas in SB006A veins are moderate to dark grey,

contain abundant protoclasts and commonly have more diffuse, wavy boundaries. SB009 also shows several thin black veinlets emerging from the thicker ones, possibly representing offshoot/injection veins (Fig. 5b). The dark grey veins in SB006A are cut and in places displaced by later quartz veins (Fig. 5c). Thin-section investigation of veins in sample SB009 (Fig. 5d, e) reveals dominant euhedral microcrystallite grains with small patches of cryptocrystalline and/or amorphous material. Partial melting textures and embayment margins are observed and point to conditions of rapid heating and cooling. There are some clasts with sharp edges and minor patches of fibrous, high interference-coloured minerals interpreted as secondary micas (e.g. sericite, chlorite) from devitrification and alteration of the original pseudotachylite (Fig. 5d, e). Near the fine-grained pseudotachylite we observe quartz, plagioclase and lesser amounts of K-feldspar and white micas. Quartz shows

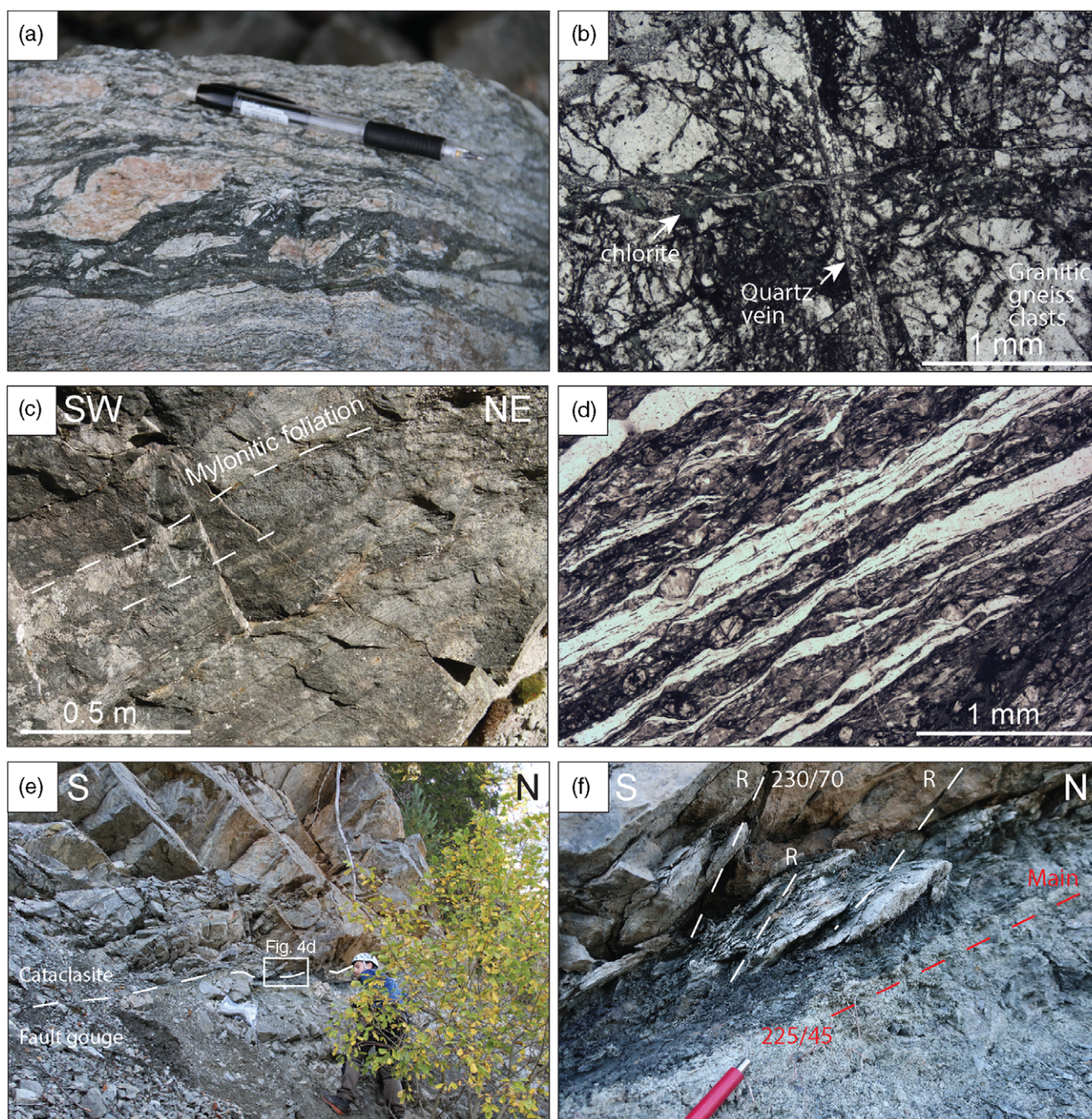


Fig. 4. (Colour online) Field, hand-specimen and thin-section photos of typical deformation rocks in the HØDZ at profile 2 (UTM33N 6632564 293914). (a, b) Cataclastic band in granitic mylonite in a loose block right next to the cliff (sample RG-16-116). (b) Photomicrograph (plane polarized) of cataclastic granite in (a). (c, d) Amphibolitic mylonite (sample RG16-101), representing the mylonitic core of the HØDZ. Mylonitic foliation (dip/dir/dip): 253/62, stretching lineation: 60→222). (d) Photomicrograph (plane polarized) of amphibolitic mylonite in (c). (e) Overview of the contact between fault gouge and overlying cataclasite. (f) Contact between fault gouge and cataclasite comprises many high-angle secondary fractures interpreted as syntectonic Riedel shears.

dominant crystal–plastic deformation, whereas feldspars are commonly cataclastically deformed. Veins in sample SB006A show some textures that are similar to those in SB009, but are more altered and deformed, indicating significant cataclastic deformation.

Hand specimen and microtextures suggest that the sampled veins represent pseudotachylites that are variably altered and deformed (Kirkpatrick & Rowe, 2013). In the remaining text we will refer to these veins as pseudotachylites, although at least some of the veins also experience significant cataclastic reworking, and a

few may be of exclusively cataclastic origin (see discussion in Section 7.b).

4. Methods

4.a. Fault gouge sample preparation

Fault gouge samples were immersed in deionized H₂O (15 MΩ) and subjected to c. 100 cycles of freezing and thawing to gently

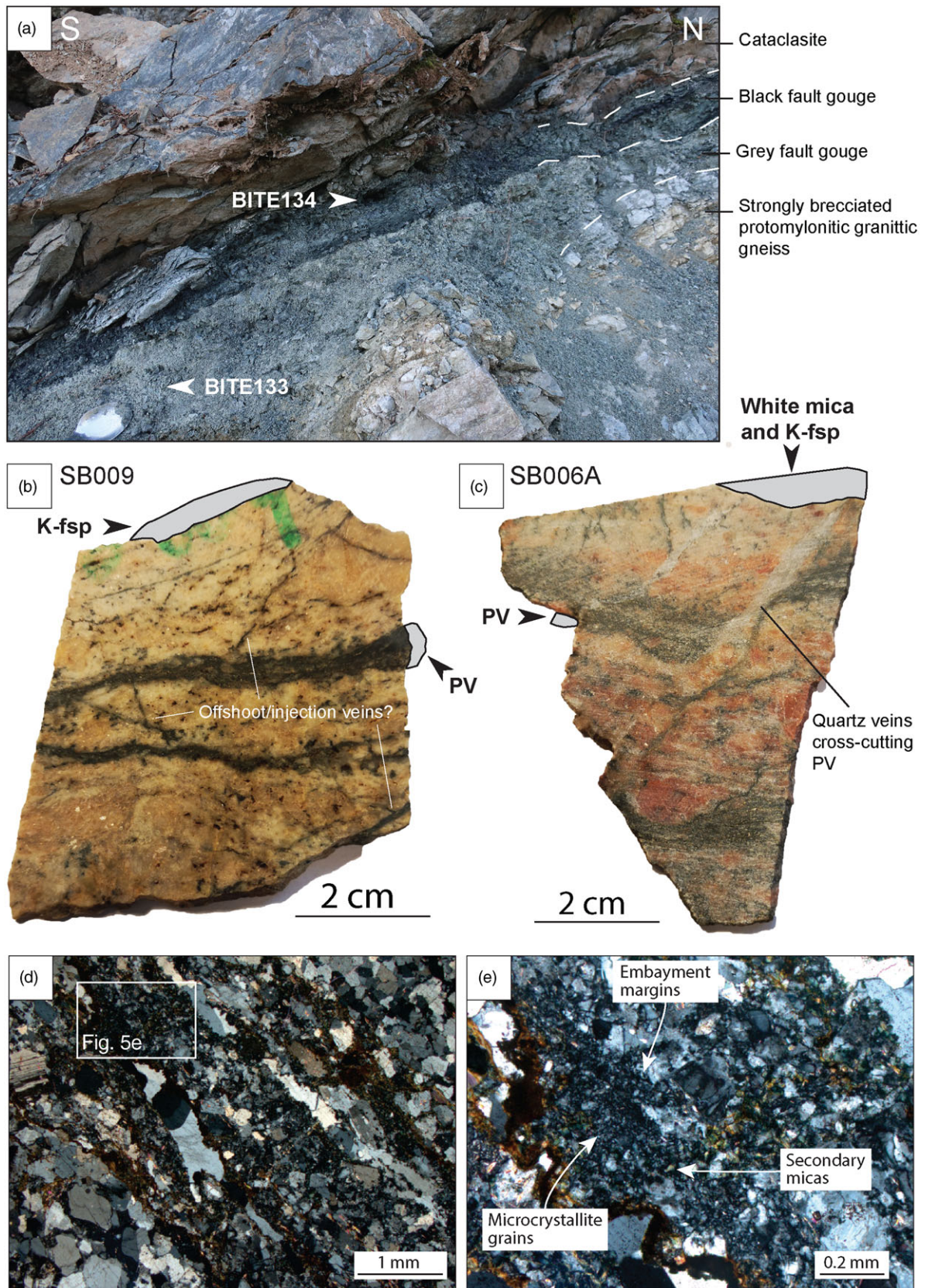


Fig. 5. (Colour online) Geochronological samples. (a) Sampling site of fault gouge samples BITE133 and BITE134 showing the textural and structural relationship between the two gouges (profile 2). (b, c) Samples for ^{40}Ar - ^{39}Ar dating (B: SB009, C: SB006A). Dated material has been extracted from the grey polygons. K-fsp = K-feldspar, PV = pseudotachylite vein. (d, e) Photomicrograph (crossed polarizers) of SB009 showing dominant euhedral microcrystallite grains with patches of cryptocrystalline and/or amorphous material, and partial melting textures and embayment margins.

disaggregate clay particles without mechanical grain-size reduction. The samples were subsequently suspended and separated into <2 μm , 2–6 μm and 6–10 μm size fractions by sinking using Stokes's law. The <2 μm fractions were separated into <0.1 μm , 0.1–0.4 μm and 0.4–2 μm fractions using a Beckman Coulter JCF-Z continuous flow centrifuge. The resulting particle size fractions were concentrated using a high-speed fixed angle rotor, and dried by freeze drying. Dried clay fractions were homogenized using an agate mortar and pestle.

4.b. X-ray diffraction

The mineralogical composition of the different grain-size fractions was studied with X-ray diffraction (XRD) using a Bruker D8 Advance diffractometer with Cu K α radiation (40 kV / 40 mA) and a Lynxeye XE detector at the Geological Survey of Norway, Trondheim. XRD scans were carried out for 3–75° 2 θ and a step size of 0.02°. Signal acquisition time was 1 s per step. The optical system was equipped with soller slits (2.5°) and a fixed divergence slit (0.6 mm). Randomly oriented specimens were run for subsequent Rietveld modelling. For accurate clay mineral identification, oriented specimens on glass slides were measured at room temperature, after glycolization for 24 hours and after heat treatment for 1 hour at 550 °C. Mineral identification was carried out with Bruker's Diffrac.EVA 4.2 using the International Centre for Diffraction Data (ICDD)'s PDF4 Minerals as well as the Crystallographic Open Database. Quantification was performed with TOPAS 5, and refined parameters included unit cell dimensions, sample displacement, preferred orientation as well as background coefficients. Limit of quantification and uncertainty is mineral-dependent, but commonly 1–2 wt % and 2–3 wt %, respectively. Illite crystallinity (Kübler Index (KI_{CIS})) was determined from the full width at half-maximum (FWHM) of the 10 Å peak and CIS-standardized according to Warr (2018) and Warr & Rice (1994).

4.c. K–Ar analysis

Splits of air-dried, homogenized clay materials and standards were packed in weighed molybdenum envelopes, and the net mass of the aliquots was determined using a Mettler Toledo XPE26DR microbalance fitted with an antistatic ionizer. The microbalance has a resolution of 2 μg and a measured reproducibility of 4 μg (1 σ). The clays and standards were left overnight in a drying oven at 85 \pm 3 °C, and then left to cool in an exicator. The molybdenum envelopes were subsequently loaded into a stainless-steel ultra-high-vacuum extraction line, and baked at a maximum temperature of 120 °C to eliminate excess water, while avoiding unwanted ⁴⁰Ar* loss from the samples, following the recommendations of Clauer & Chaudhuri (1995).

Argon was extracted from the aliquots for 20 min at 1400 °C in a Pond Engineering double vacuum resistance furnace. During heating, bulk sample gas was expanded directly into a stainless-steel vessel housing a freshly activated Titanium Sublimation Pump, to strip the sample gas from a majority of reactive gases including H₂O, N, O, CO and CO₂ (O'Hanlon, 2005). Purified sample gas was spiked with a known amount (c. 2×10^{-13} moles) of pure ³⁸Ar spike (Schumacher, 1975) and equilibrated for 2 min. The gas mixture was subsequently isolated in a second clean-up stage and exposed for 10 min to two SAES GP50 getter cartridges with ST101 Zr–Al alloy, one of which was kept at 350 °C and one at room temperature, to remove residual reactive gases including H₂ and CH₄.

Argon isotopes were determined on an IsotopX NGX multicollector noble gas mass spectrometer using faraday cups fitted with 1012 Ω amplifiers, except for ⁴⁰Ar which was measured using a faraday fitted with a 1011 Ω amplifier. Time-zero beam intensities were measured for 30 cycles of 20 1-s integrations, and time-zero intensities were calculated using exponential regressions back to gas inlet time. Furnace blanks were run regularly between samples, and had Ar compositions comparable to atmospheric argon. Instrument mass discrimination was determined within this analytical batch by a comparing a weighted mean of 50 analyses of atmospheric argon (⁴⁰Ar/³⁶Ar = 299.579 \pm 0.012) with the reference value of 298.56 \pm 0.31 (Lee *et al.* 2006). The ³⁸Ar spike pipette was calibrated using GA-1550 biotite with ⁴⁰Ar* = 1.342 \pm 0.007 $\times 10^{-9}$ mol g⁻¹ (McDougall & Wellman, 2011) and HD-B1 biotite (Fuhrmann *et al.* 1987) with a ⁴⁰Ar* = 3.351 \pm 0.01 $\times 10^{-10}$ mol g⁻¹ (Charbit *et al.* 1998). The overall standard deviation of the pooled spike calibrations by combined GA1550 and HD-B1 is <0.3 %. The accuracy of the ⁴⁰Ar* determinations was monitored within-run by HD-B1 biotite.

Potassium concentration was determined by digesting a sample aliquot of ~50 mg of sample material in Li2B4O7 flux at a temperature of 1000 \pm 50 °C in palladium crucibles. The resulting glass was subsequently dissolved in HNO₃, and analysed on an Agilent 5110 VDV ICP-OES. 1 σ uncertainties depend on the sample weight and its K concentration, and are typically 1.5 % relative for pure mica, as determined by repeated measurements of geological standards DNC dolerite, Mica-Mg phlogopite and MA-N granite.

K–Ar ages were calculated using the ⁴⁰K decay constants, abundance and branching ratio of Steiger & Jäger (1977). Atmospheric argon corrections were performed using the relative abundances of ⁴⁰Ar, ³⁸Ar and ³⁶Ar of Lee *et al.* (2006; ⁴⁰Ar/³⁶Ar = 298.56 \pm 0.31). 1 σ uncertainties were estimated using the error equation for multicollector isotope dilution measurements from Hałas & Wójtowicz (2014) modified to take into account the uncertainty on mass discrimination.

4.d. ⁴⁰Ar–³⁹Ar analysis

The samples were cut into slabs, c. 0.3–0.5 cm thick. A micro rotary tool was then used under flowing water to cut ~0.2 cm³ chips from the pseudotachylites (see Fig. 5b, c for sampling sites). The vein chips were further crushed with a mortar. Care was taken not to include larger host rock fragment entrained in the melt matrix; however, this possibility cannot be ruled out. In particular, the pseudotachylite in sample SB006A was less defined (thinner) and harder to separate from the host rock fragments (Fig. 5c). From the same rock slabs, host rock micas and feldspars were separated applying normal methods. The analytical protocol follows Vissers *et al.* (2020). The raw blank-corrected mass spectrometer outputs can be found in Table S1 in the Supplementary Material available online at <https://doi.org/10.1017/S0016756822000966>, and the main results in Table 3 (further below).

5. Results

5.a. Fault gouge mineralogy

All three fault gouge samples from the Himdalen Fault contain dominant illite/muscovite, chlorite and smectite (Table 1; XRD spectra in Fig. S2 in the Supplementary Material available online at <https://doi.org/10.1017/S0016756822000966>). Although small amounts of K-feldspar are present in the three coarsest fractions

Table 1. XRD results (wt %), including illite crystallinity (Kübler Index KI_{CIS})

Sample	Fraction (μm)	ill/musc	K-fsp	chl	sm	qtz	plag	ant	cal	rt	GOF	Rwp	$KI_{CIS}(\Delta 2^\circ)$
BITE133	<0.1	Not enough material											
	0.1–0.4	38		12	50						1.62	17.84	0.74
	0.4–2	45		9	29		17				1.49	17.94	0.64
	2–6	27		7	16	1	43		4	2	1.32	16.97	0.56
	6–10	20		8	16	2	48		4	2	1.36	18.02	0.36
BITE134	<0.1	xxxx		xxx	xx								1.85
	0.1–0.4	64		16	20						1.64	19.51	1.41
	0.4–2	58	t	15	20	7					1.47	18.73	0.99
	2–6	40	3	10	13	31		3			1.39	18.09	0.88
	6–10	34	4	9	12	38		3			1.33	18.22	1.08
BITE135	<0.1	Not enough material											
	0.1–0.4*	45		33	20	2					2.36	12.44	1.42
	0.4–2	29	4	30	33	4					2.84	15.42	0.79
	2–6	29	9	28	26	8					2.8	15.44	0.64
	6–10	25	13	21	26	10	5				2.72	15.26	0.46

Notes: Mineral abbreviations: ill/musc, illite/muscovite; K-fsp, alkali-feldspar; chl, chlorite; sm, smectite; qtz, quartz; plag, plagioclase; ant, anatase; cal, calcite; rt, rutile; GOF, goodness of fit; Rwp, weighted profile factor. Both GOF and Rwp represent accuracy parameters for mineral quantification by Rietveld modelling.

*Concentrations are only approximate, due to poor sample crystallinity. Smectite concentration is most likely underestimated.

Table 2. K–Ar fault gouge results

Sample	Fraction (μm)	$^{40}\text{Ar}^*$ (mol g^{-1})	σ (%)	$^{40}\text{Ar}^*$ (%)	K (wt %)	σ (%)	Age (Ma)	σ (Ma)
BITE133	<0.1	4.7002E-10	0.42	50.7	1.306	3.2	196.5	± 6.3
	0.1–0.4	1.0790E-09	0.44	73.0	1.874	1.8	304.7	± 5.7
	0.4–2	1.8863E-09	0.31	85.7	2.652	1.6	369.6	± 6.0
	2_6	1.9102E-09	0.33	92.2	2.640	1.6	375.4	± 6.1
	6_10	1.7219E-09	0.37	92.4	2.343	1.7	380.6	± 6.6
BITE134	<0.1	9.776E-10	0.38	80.0	2.596	1.7	205.0	± 3.5
	0.1–0.4	1.557E-09	0.28	87.1	3.423	1.5	244.9	± 3.8
	0.4–2	1.813E-09	0.39	91.1	3.556	1.5	272.4	± 4.1
	2–6	1.631E-09	0.33	92.4	3.207	1.5	271.8	± 4.2
	6–10	1.563E-09	0.39	92.7	3.168	1.5	264.2	± 4.2
BITE135	<0.1	4.2756E-10	0.40	49.5	1.192	1.6	195.8	± 3.2
	0.1–0.4	7.7211E-10	0.35	54.6	1.759	1.5	236.9	± 3.7
	0.4–0.2	1.1804E-09	0.29	66.0	2.245	1.5	280.3	± 4.3
	2–6	2.0646E-09	0.29	78.7	3.205	1.5	337.7	± 5.2
	6–10	2.6831E-09	0.29	87.3	3.583	1.5	387.2	± 6.0

of BITE134 and BITE135, illite/muscovite is the only K-bearing phase in the two finest size fractions of all three samples. Quartz is present in moderate to minor amounts in the coarser fractions of all three samples, whereas significant concentrations of plagioclase are only present in BITE133. The difference in content of wall-rock derived plagioclase between BITE133 and BITE134 is consistent with the observed contrast in fault gouge characteristics, wherein BITE134 is significantly finer-grained than BITE133 and contains no observable wall rock fragments. Minor to trace

amounts of K-feldspar are present in the coarsest fractions of BITE134 and BITE135.

The crystallinity of illite varies significantly within each sample from anchizone (KI_{CIS} of 0.36) to early diagenetic (KI_{CIS} of 1.85; Table 1). The KI is strongly positively correlated with grain size, where illite in the coarser size fractions has higher crystallinity than in the finer size fractions. Notably, illite in the coarsest size fractions of samples BITE133 and BITE134 has significantly different KI values ($KI_{CIS} = 0.88\text{--}1.08$ vs $0.36\text{--}0.64$, respectively; Table 1),

Table 3. ^{40}Ar – ^{39}Ar results

Sample	Material	Steps (n)	% ^{39}Ar	Age $\pm 1.96\sigma$	Spectrum		Inverse isochron		Spread (%)
					MSWD (P)	Age $\pm 1.96\sigma$	MSWD (P)	Trapped ^{40}Ar – ^{36}Ar	
SB006A	K-fsp (myl.)	4–8(5)	75.88	435.43 \pm 23.83	0.74(0.56)	284.45 \pm 488.88	0.05(0.98)	1854.56 \pm 10441.86	8.3
SB006A	White mica (myl.)	6–18(13)	72.97	908.62 \pm 7.04	1.17(0.30)	866.65 \pm 62.93	0.34(0.98)	21453.14 \pm 463797.67	8.9
SB006A	Pseudotachylite	2–5(4)	33.77	375.02 \pm 22.71	0.60(0.61)	381.07 \pm 53.95	0.89(0.41)	276.37 \pm 228.73	12.4
SB006A	Pseudotachylite	8–16(9)	33.04	639.5 \pm 18.8	1.169 (0.31)				
SB009	K-fsp (myl.)	2–5(4)	37.23	430.4 \pm 20.3	11.283(0.00)	344.5 \pm 131.8	0.155(0.85)	2040.0 \pm 3143.2	10.7
SB009	Pseudotachylite	4–7(4)	31.27	351.66 \pm 4.44	0.89(0.44)	272.67 \pm 131.20	0.49(0.61)	–33394.64 \pm 4322414.13	3.4
SB009	Pseudotachylite	11–20(10)	36.56	294.61 \pm 5.15	0.58(0.81)	283.07 \pm 19.85	0.40(0.92)	504.84 \pm 435.76	7.8

although the samples were collected only 10 cm from each other. The KI values of the coarsest fractions in BITE135 are comparable to those in BITE133.

Qualitative assessment of illite polytypes (2M1 and 1M-1Md; Velde, 1965) shows that all size fractions are dominated by poorly crystalline 1M illite. Size fraction 0.1–0.4 μm in BITE135 also contains minor amounts of smectitic interlayers in the illite. Well-ordered 2M1 illite is subordinate in the coarsest fraction (6–10 μm) of BITE135, as evidenced by a minor peak at 2.8 \AA (Fig. S2 in the Supplementary Material available online at <https://doi.org/10.1017/S0016756822000966>; Grathoff & Moore, 1996). The predominance of low-temperature, disordered 1M illite is consistent with anchizone- to early diagenetic-grade illite crystallinities (Table 1). The 1M illite likely formed by dissolution of wall-rock-derived K-feldspar (Haines & van der Pluijm, 2012).

5.b. K–Ar fault gouge ages

A total of 15 K–Ar ages were obtained from the three Himdalen Fault gouge samples (Table 2). All fractions have moderate K concentrations (from 1.192 to 3.583 wt %) and the Ar is dominantly radiogenic (49.5 to 92.7 %). The ages vary from 387.2 \pm 6.0 Ma to 195.8 \pm 6.3 Ma, and all samples show consistently decreasing ages with grain size. The finest size fractions (<0.1 μm) of all samples have nearly identical ages (from 195.8 \pm 3.2 to 205.0 \pm 3.5 Ma), and the coarsest fractions for BITE133 and BITE135 overlap within error (380.6 \pm 6.6 and 387.2 \pm 6.0 Ma). The ages of the three coarsest fractions both in BITE134 and BITE133 are identical within error at c. 268 Ma and c. 375 Ma, respectively.

5.c. ^{40}Ar – ^{39}Ar ages

White mica and K-feldspar from sample SB006A (host rock) defines overlapping age steps of parts of the degassing spectrum (Fig. 6a) and yielded inverse variance weighted means of 908.6 \pm 7.0 Ma and 435.4 \pm 23.8 Ma, respectively (Table 3). The degassing spectrum from the pseudotachylite of this sample (Fig. 6b) shows two mini-plateaus of 375.0 \pm 22.7 Ma and 639.5 \pm 18.8 Ma, respectively.

Host rock K-feldspar from sample SB009 reveals a disrupted age pattern (Fig. 6d); however, steps 2–5 hint at a resemblance to samples SB006A (430.5 \pm 20.3 Ma; Fig. 6b), although the statistical basis for this is poor. The pseudotachylite samples reveal two mini-plateaus, one at 351.7 \pm 4.4 Ma and the other at 294.6 \pm 5.2 Ma at higher-temperature steps (Fig. 6e).

In both pseudotachylite samples, there are distinct younger age populations compared to the host rock samples. Both carry a late Devonian signal (375.0 \pm 22.7 Ma and 351.7 \pm 4.4 Ma), both of which are statistically within error. However, they behave differently at higher-temperature steps. Sample SB006A climbs to c. 640 Ma, whereas SB009 defines a clear plateau at c. 295 Ma. We speculate whether this up-climbing pattern in sample SB006A could be due to the presence of a higher portion (mix) of unmelted material from the source rock with different diffusive properties as seen in many other natural pseudotachylites (e.g. Di Vincenzo *et al.* 2004). The Ca/K data (calculated from ^{37}Ar – $^{39}\text{Ar}_k$; Fig. 6c) indicate at least two Ar reservoirs, from high Ca/K ratios (e.g. plagioclase) to low ratios. Sample SB009 drops down to a plateau of 294.6 \pm 5.2 Ma (Fig. 6e). Judging from the Ca/K data for this sample, the gas comes from high-K reservoirs, probably host-rock K-feldspar (351.7 \pm 4.4 Ma) and a melt-matrix-dominated reservoir (294.6 \pm 5.2 Ma).

6. Discussion

The presented structural and geochronological results show that the HØDZ is a multi-reactivated deformation zone where repeated brittle deformation events have exploited and partly overprinted an older mylonitic fabric associated with the Ørje Shear Zone. Below we first interpret the K–Ar geochronological dataset, before discussing the regional implications of the new deformation ages. A brief discussion of brittle localization in visco-plastic shear zones follows at the end.

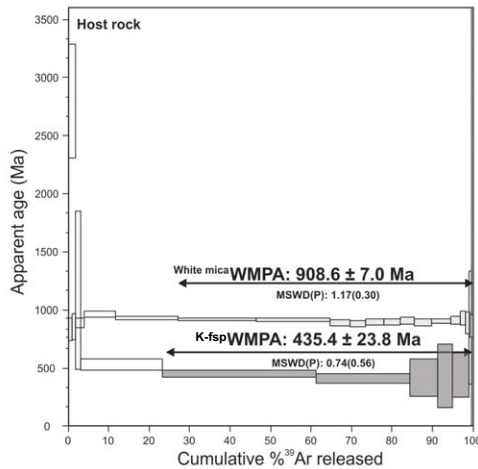
6.a. Interpreting K–Ar geochronological data of a multi-reactivated fault

K–Ar fault gouge dating is not a straightforward geochronological method but requires careful analyses of each individual sample through integration of the isotope data with other constraints, such as field and microscopic observations, mineralogical quantification and external geochronometers and geothermometers (van der Pluijm *et al.* 2001; Zwingmann & Mancktelow, 2004; Haines & van der Pluijm, 2008; Viola *et al.* 2016; Vrolijk *et al.* 2018; Scheiber *et al.* 2019; Mottram *et al.* 2020; Tartaglia *et al.* 2020; Hueck *et al.* 2022; Viola *et al.* 2022). Below we discuss why we interpret the HØDZ fault gouge geochronological results to constrain faulting at c. 380, c. 270 and c. 200 Ma.

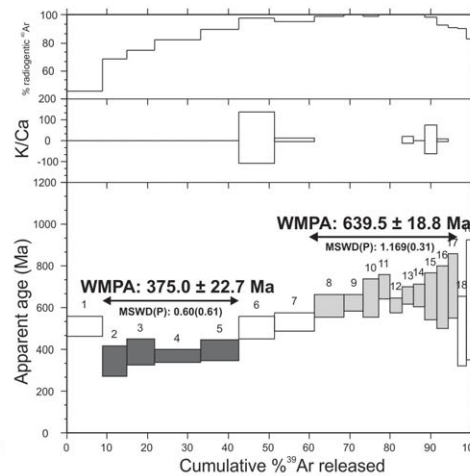
The most robust constraint on the absolute timing of fault activity along the Himdalen Fault is represented by the ages of the finest

SB006A

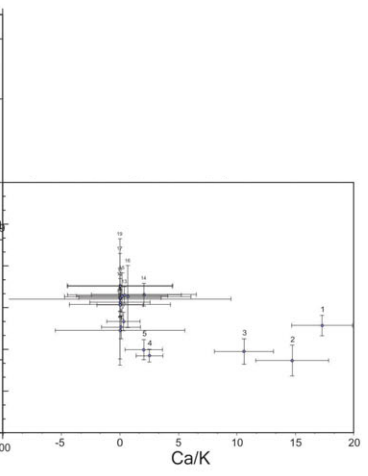
(a) K-feldspar/White mica

**SB006A**

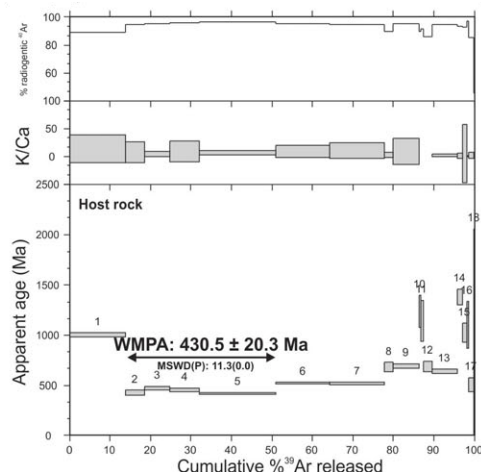
(b) Pseudotachylite-Ultracataclasite veins (PUV)



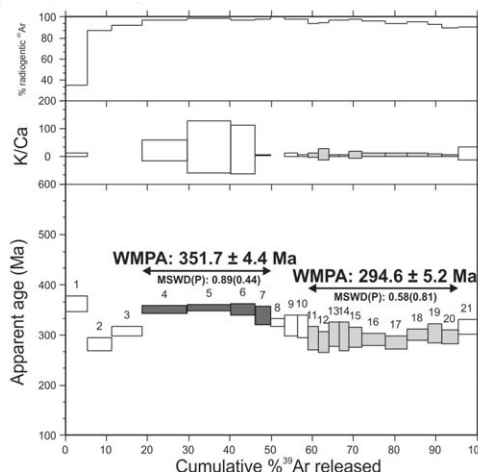
(c) PUV (Ca/K vs. Age)

**SB009**

(d) K-feldspar

**SB009**

(e) Pseudotachylite-Ultracataclasite veins (PUV)



(f) PUV (Ca/K vs. Age)

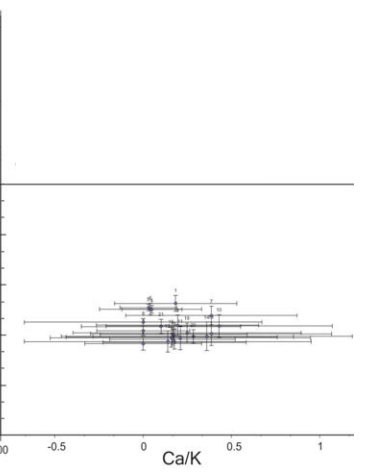


Fig. 6. ^{40}Ar - ^{39}Ar degassing spectra (a, b, d, e), with Ca/K vs. age plots (c and f) for the pseudotachylite vein analyses.

size fraction ($<0.1\ \mu\text{m}$) in all three gouge samples, which are nearly identical within error at $196.5 \pm 6.3\ \text{Ma}$, $205.0 \pm 3.5\ \text{Ma}$ and $195.8 \pm 3.2\ \text{Ma}$ (BITE133, 134 and 135, respectively; Table 2; Fig. 7). The obtained age of the finest fraction ($<0.1\ \mu\text{m}$) is commonly interpreted as the age of the last datable increment of faulting, as this fraction contains dominantly authigenic syn-kinematic illite (e.g. Zwingmann *et al.* 2004; Wemmer *et al.* 2011; Ksienzyk *et al.* 2016). The finest fraction may contain traces of inherited grains, but only in very rare cases do these contribute significantly to the obtained K-Ar age (e.g. Viola *et al.* 2018). Typically, the most common contaminant in the finest size fraction is wall-rock-derived 2M1 illite/muscovite. Its effect on the obtained age may be corrected for by the Illite Age Analysis approach (IAA; Pevar, 1999; van der Pluijm *et al.* 2001). However, the samples presented in this study almost exclusively comprise poorly crystalline, authigenic 1M illite (Table 1; Fig. S2 in the Supplementary Material available online at [https://](https://doi.org/10.1017/S0016756822000966)

doi.org/10.1017/S0016756822000966), which precludes the use of IAA. The fact that all three samples converge to a similar age for their finest size fraction is a strong argument for interpreting this age (c. 200 Ma) as geologically meaningful. Conservatively, this age should be regarded as a maximum age of the last period of fault slip (e.g. Zwingmann & Mancktelow, 2004; Tartaglia *et al.* 2020).

The c. 200 Ma faulting event is not the only activity recorded by the Himdalen Fault. The field relationships disclose a multiphase brittle history with a distinct difference in character between the grey, fragment-rich gouges (BITE133 and 135) and the black, fine-grained gouge (BITE134; Fig. 5a). The latter appears more deformed and contains much more illite than the former. The apparent overprinting relationship of the black gouge at the expense of the grey at profile 2 (Figs. 2, 5a) suggests that the black gouge partially reworked the former by continued crushing and mineral transformations. Similar situations of partial reactivation and overprinting of fault gouges have been documented in several

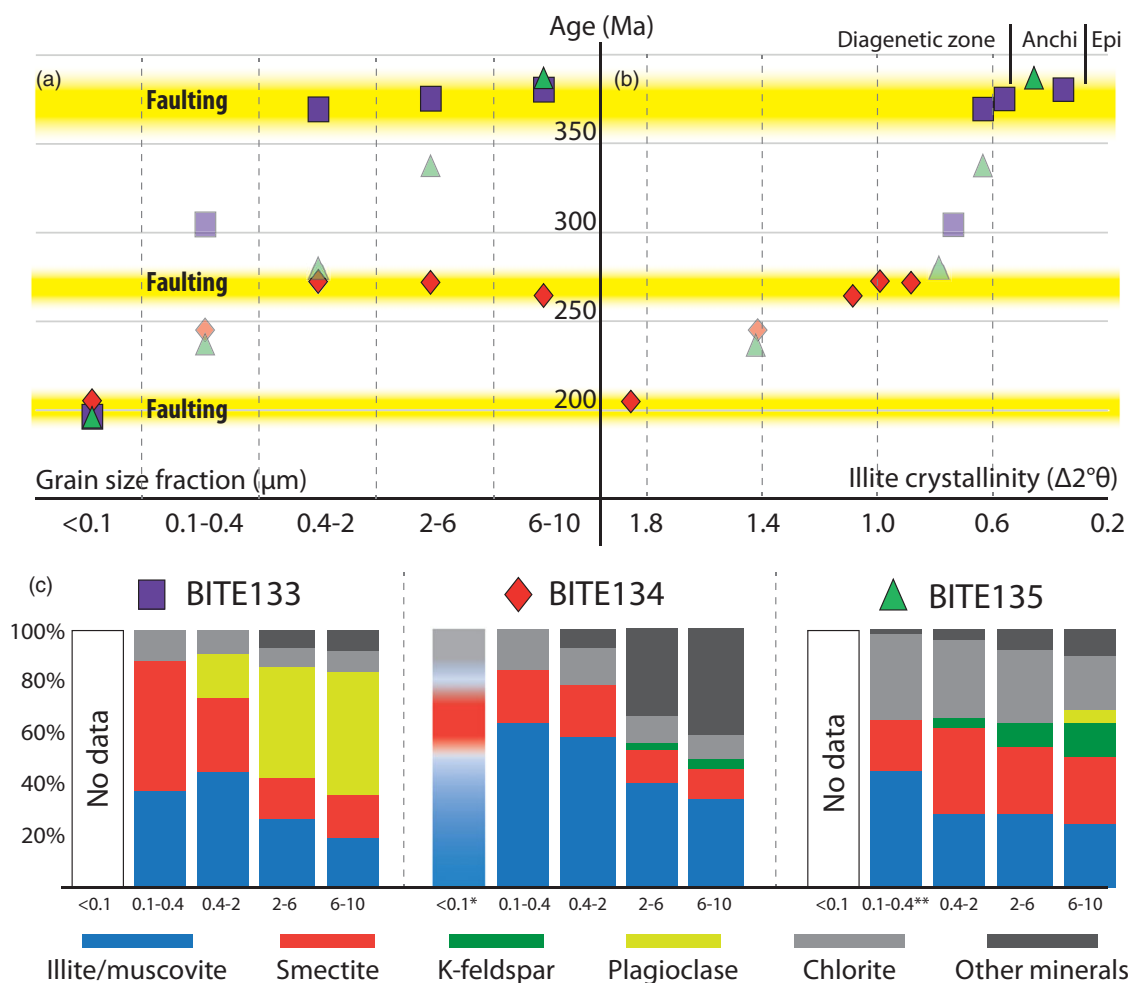


Fig. 7. (Colour online) Compilation of K–Ar and XRD analyses of the fault gouges. (a) Age vs grain-size plot. Solid marker: interpreted as geologically significant; transparent marker: interpreted as a mixed age and therefore geologically insignificant. (b) Age vs illite crystallinity ($\Delta 2\theta$). Yellow horizontal bars indicate the interpreted faulting events recorded by the fault gouge samples. (c) Mineralogy of the dated samples. Notes on XRD-columns: <0.1 μm fractions in samples BITE133 and BITE135 do not yield enough material for XRD analysis. * Analysed in low-background Si-sample holders with depressions. **Concentrations are only approximate due to poor sample crystallinity. Smectite concentration is most likely underestimated.

other fault zones (Viola *et al.* 2013, 2022; Torgersen *et al.* 2015a; Tartaglia *et al.* 2020). This first-order relative age difference is supported by the presence of significant amounts of wall-rock-derived minerals (e.g. plagioclase) in the three coarsest fractions of BITE133, but not in the overprinting BITE134 (Table 2; Fig. 7).

Although the three fault gouges show a common age for the finest fraction, reflecting that they all experienced significant new illite growth during the latest datable reactivation event, the timing of their initial development differs. The observed relative age difference between BITE133 and BITE134 is recorded by the K–Ar ages of the three coarsest fractions in both samples: the black gouge (BITE134) is about 100–110 Ma younger than the neighbouring grey gouge (BITE133). BITE134, in turn, overlaps with the 6–10 μm fraction age of BITE135 (Table 2; Fig. 7). Age plateaus in K–Ar age-versus-grain-size space, termed pseudo-plateau ages, are defined by two or more neighbouring size fractions with the same age and are observed in many fault-dating studies (Torgersen *et al.* 2015a; Aldega *et al.* 2019; Scheiber *et al.* 2019). Pseudo-plateau ages indicate that the fault gouge contains a significant population of mineral grains with similar age, and therefore pseudo-plateau ages can be interpreted as robust and geologically significant (Scheiber *et al.* 2019).

It has previously been proposed that the coarsest fractions of fault gouges consist predominantly of protolithic minerals inherited from the wall rocks (e.g. van der Pluijm *et al.* 2001). However, several recent studies show that in multi-reactivated fault gouges, the coarsest fractions may be dominated by authigenic, syn-kinematic minerals (herein called *proto-authigenic* minerals) that are associated with an earlier faulting phase than that recorded by the finest size fraction (Torgersen *et al.* 2015a; Ksienzyk *et al.* 2016; Viola *et al.* 2016; Kemp *et al.* 2019). The obtained ages of the coarsest fractions should therefore be carefully evaluated with regard to the dominance of either protolithic or proto-authigenic minerals, or a mixture between them. To do so, several factors must be considered, including (a) which K-bearing mineral phases are present, (b) the amount of each mineral, (c) their K-content, (d) whether they are wall-rock-derived or authigenic, (e) their theoretical K–Ar closure temperature and (f) the approximate temperatures during faulting.

Illite/muscovite is the dominant contributor to the obtained K–Ar ages of the coarsest fractions in all three samples (Table 1). If the illite/muscovite was well-ordered 2M1 muscovite derived from the host mylonites (i.e. protolithic grains), the age should approach that constrained by the ^{40}Ar – ^{39}Ar date of

908.6 ± 7.0 Ma (Table 3; Fig. 6). However, the samples contain no 2M1 illite/muscovite and the anchizone to diagenetic zone KI values (Table 1; Fig. S2 in the Supplementary Material available online at <https://doi.org/10.1017/S0016756822000966>; Fig. 7) strongly suggest that the illite/muscovite is authigenic. We therefore interpret the pseudo-plateau ages of BITE133 and BITE134 (*c.* 375 Ma and 268 Ma, respectively) to date syn-kinematic, authigenic illite/muscovite formed during two significant faulting episodes. The difference in age correlates with a shift in illite crystallinity between the black gouge fractions ($KI_{CIS} = 0.88\text{--}1.08$) and those from the grey gouges ($KI_{CIS} = 0.36\text{--}0.64$; Table 1; Fig. 7). This shift indicates that the fault reactivation event leading to the development of the black gouge likely took place at lower temperatures than the faulting episode causing the formation of the grey gouges. At the same time, this is significantly higher than that of the younger (*c.* 200 Ma) finest fraction ($KI_{CIS} = 1.85$).

It should be noted here that it is a very common phenomenon that the Kübler Index, i.e. the FWHM of the (001) illite peak, increases with decreasing grain size. This means that the highest KI values are recorded for the <0.1 µm fraction and often they are automatically assigned diagenetic formation conditions (Schomberg *et al.* 2019). At such small grain sizes, however, peak broadening is frequently observed and results from small crystallite sizes. The question arises whether formation conditions can be interpreted from the KI values of the finest size fractions (<<2 µm), or if increased KI values for these size fractions are solely because the grains are smaller. Independent temperature (and pressure) constraints such as fluid inclusion analyses would be very useful in future studies to confirm the assumptions derived from KI values.

The pseudo-plateau ages may be affected by the presence of K-feldspar and/or plagioclase, which are present in variable amounts in all three samples. BITE134 and BITE135 contain <5 wt % and <13 wt %, respectively, of mainly K-feldspar (Table 1). $^{40}\text{Ar}\text{--}^{39}\text{Ar}$ dating of K-feldspar from the host rock shows that these have significantly older Ar ages than the fault gouges (435.4 ± 23.8 Ma and 430.2 ± 20.3 Ma; Table 3; Fig. 6), suggesting that either (1) their effect on the obtained K–Ar ages is insignificant or (2) they crystallized or were isotopically reset at the same time as the illite. BITE133 contains noteworthy amounts of plagioclase (17–48 wt %; Table 1). Although plagioclase usually contains only trace amounts of K it may comprise up to 1 % K (e.g. Heier, 1962), which means that contribution of plagioclase to the age cannot be completely ruled out without further analysis. However, given that the three coarsest fractions of BITE133 overlap in age despite a large variation in plagioclase content (17–48 wt %), and that its pseudo-plateau age overlaps with the age of the coarsest fraction in BITE135 (Fig. 7), as well as with the $^{40}\text{Ar}\text{--}^{39}\text{Ar}$ plateau age of pseudotachylite in sample SB006A (Fig. 6), it is very unlikely that plagioclase contributes significantly to the age of these grain-size fractions. We therefore interpret the pseudo-plateau ages in the HØDZ fault gouges to represent significant faulting events at *c.* 380 Ma and *c.* 270 Ma (Fig. 7).

6.b. Interpretation of $^{40}\text{Ar}\text{--}^{39}\text{Ar}$ pseudotachylite ages

The dated pseudotachylites show two-plateau degassing spectra with similar ages for the low-temperature steps (375.0 ± 22.7 Ma and 351.7 ± 4.4 Ma), but different ages for the high-temperature steps (294.6 ± 5.2 Ma and 639.5 ± 18.8 Ma; Fig. 6; Table 3). Most of the pseudotachylite plateau ages are significantly younger than those in the host rock, which matches well the cross-cutting nature of the pseudotachylites (Fig. 5b, c) and

strongly indicates that these plateau ages date deformation rather than regional cooling.

One of the plateau ages, at *c.* 640 Ma (SB006A), is older than K-feldspar in the host mylonites (*c.* 435 Ma) and, thus, likely to represent an inherited component or mix of components, possibly also partially reset. Such an interpretation is consistent with the presence of significant protoclads in the SB006A pseudotachylites (Fig. 5b, c). SB009, which do not have a *c.* 640 Ma age signal, also contains significantly fewer protoclads. An alternative interpretation is that the *c.* 640 Ma plateau age dates cataclastic deformation of the mylonite that was in turn reworked by the pseudotachylites. Such an interpretation is consistent with the widespread cataclastic deformation textures both at outcrop and microscale but requires that the dated vein material has a higher closure temperature than K-feldspars in the mylonites. Such material could possibly be syn-deformational crystallized micas and/or partially melted micas.

The three remaining plateaus constrain, within error, two age groups (380–350 Ma and *c.* 295 Ma). Based on field observation, microscale textures and geochronological data, we suggest that the two ages are of different origin – pseudotachylite and cataclasisite.

The main argument in favour of such an interpretation comes from the age spectrum of SB009. Here the high-temperature steps (11–20) constrain a younger plateau age (*c.* 295 Ma) than the lower-temperature plateau (4–7; *c.* 350 Ma; Fig. 5e), which suggests that the *c.* 295 Ma signal originates from a more retentive source than the *c.* 350 Ma signal. We interpret the two sources to be melt-dominated and cataclastic-dominated matrix, respectively, which is consistent with hand specimen and microscale textures and structures typical for both pseudotachylite and cataclasisite (Fig. 5b–e). The existence of an episode of significant cataclastic deformation pre-dating pseudotachylite formation is also supported by the fact that the plateau ages of SB009 and SB006A overlap internally (Fig. 6b, e), as well as with the K–Ar ages of the coarsest size fractions of the two fragment-rich fault gouges (BITE133 and 135; Fig. 7).

Sherlock *et al.* (2009) suggest that cataclasisites are unsuitable for argon dating because they are only mechanically crushed and therefore not outgassed. However, recent studies have shown that cataclastic deformation may comprise considerable authigenic mineral growth (e.g. Schleicher *et al.* 2015; Gundlach-Graham *et al.* 2018) and cause considerably increased Ar diffusivity, which may lead to complete resetting of the Ar system (e.g. in K-feldspar; Wang *et al.* 2020). In the case of the HØDZ, feldspars in and around the pseudotachylites show significant fracturing and cataclastic deformation (Fig. 5d, e). Dissolution of fractured feldspar may lead to precipitation of poorly crystalline 1M illite (Haines & van der Pluijm, 2012). Indeed, authigenic mineral growth is documented in the HØDZ by the predominance of 1M illite in the coarse fault gouge fractions with ages around 380 Ma (Table 1; Fig. S2 in the Supplementary Material available online at <https://doi.org/10.1017/S0016756822000966>).

In summary, the pseudotachylite age spectra are complex, and a unique interpretation is not possible from the presented data alone. The most consistent and plausible interpretation is that the $^{40}\text{Ar}\text{--}^{39}\text{Ar}$ plateau ages date early cataclastic deformation around 380–350 Ma and pseudotachylite formation at 294.6 ± 5.2 Ma. Field, hand specimen and microscale observations demonstrate widely distributed cataclastic deformation that is cut by pseudotachylite veins (Figs. 4a, b, 5b, c). The interpretation implies that only SB009 pseudotachylite preserves enough material to resolve a *c.* 295 Ma frictional melting–cooling event.

6.c. Regional implication of the new deformation ages

The HØDZ has accommodated multiple deformation events at different conditions, separated by millions of years of inactivity. It therefore provides a 700 Ma archive of crustal deformation in southeast Norway, which is discussed below and summarized in Figure 7.

6.c.1. Early Neoproterozoic greenschist facies extensional reactivation (Fig. 8a)

The oldest deformation rocks within the HØDZ are the mylonites making up the Ørje Shear Zone. ^{40}Ar – ^{39}Ar dating of white mica from these mylonites gives an age of 908.6 ± 7.0 Ma (Figs 6, 8). This age overlaps with ^{40}Ar – ^{39}Ar ages from other large shear zones within the Sveconorwegian Orogen (Fig. 8a), such as the Mylonite Zone (*c.* 922–860 Ma; Viola *et al.* 2011) and the Kristiansand–Porsgrunn Shear Zone (*c.* 890–880 Ma; Mulch *et al.* 2005). These deformation ages are invariably interpreted to date late-orogenic extensional reactivation of pre-existing compressional shear zones. We suggest a similar interpretation of the HØDZ white mica age. Given its parallelism to the northern segment of the Mylonite Zone, it likely also accommodated sinistral oblique top-to-the-W slip during this event (Fig. 8a; Viola *et al.* 2011).

6.c.2. Late Neoproterozoic activity?

During the late Neoproterozoic break-up of Rodinia, major brittle deformation led to the development of multiple rift basins in Baltica (Kumpulainen & Nystuen, 1985). The ^{40}Ar – ^{39}Ar plateau age of 639.5 ± 18.8 Ma from one of the pseudotachylites overlaps with the timing of this major rifting event (Pease *et al.* 2008; Kjøl, 2020), indicating that the HØDZ may have been active at this time interval. However, the geological significance of the *c.* 640 Ma age is highly uncertain (as described in Section 7.b. above) and more structural–geochronological analysis of the HØDZ is required to verify its possible late Neoproterozoic deformation history.

6.c.3. Silurian cooling ages associated with the Caledonian orogeny (Fig. 8b)

The HØDZ seems largely unaffected by the Caledonian orogeny (*c.* 480–400 Ma; Corfu *et al.* 2014), although the study site sits close to the easternmost extent of the Caledonian front. The only ‘Caledonian’ ages in the HØDZ come from K-feldspar in the mylonites (Table 3; Fig. 6). Although the ^{40}Ar – ^{39}Ar plateau ages of both K-feldspar samples have large errors (435.4 ± 23.8 Ma and 430.2 ± 20.3 Ma), they are similar to the stratigraphically constrained Wenlock–Ludlow age (*c.* 430–420 Ma) of major Caledonian contraction in the Osen – Røa Nappe Complex within the Oslo Graben (Fig. 8b; Bruton *et al.* 2010). However, it is considered highly unlikely that the HØDZ accommodated any Caledonian strain as it is oriented nearly parallel to the main Caledonian ESE transport direction in this area. We therefore interpret the *c.* 435 Ma K-feldspar ages as cooling ages linked to the effects of the advancing and collapsing Caledonian orogen.

6.c.4. Late Devonian – Early Carboniferous brittle reactivation (Fig. 8b)

The most unexpected deformation ages obtained in this study are the Late Devonian to Early Carboniferous ^{40}Ar – ^{39}Ar plateau ages of the pseudotachylites and the K–Ar ages of the coarsest fraction of two of the fault gouges (385–350 Ma; Figs. 6–8). There are very few similar metamorphic or deformation ages in southeast Norway

and southern Sweden. The only exceptions are a number of slickensided fracture surfaces at Forsmark, eastern Sweden, which give Rb–Sr isochrons between 398.6 ± 5.1 Ma and 348.9 ± 8.6 Ma (Tillberg *et al.* 2020), and a series of metamict zircons in central Sweden with a lower intercept U–Pb discordia age of 384 ± 15 Ma (Fig. 8b; Högdahl *et al.* 2001). In Baltica, the major tectonic event at that time was the collapse of the Scandinavian Caledonides. The collapse took place through several stages along dominating NW–SE to E–W extension directions (Osmundsen & Andersen, 2001; Fossen, 2010; Braathen *et al.* 2018; Wiest *et al.* 2021), and is particularly well recorded by the large extensional detachment zones and supradetachment basins in western Norway (e.g. Osmundsen & Andersen, 2001). Alkali feldspar ^{40}Ar – ^{39}Ar thermochronology points toward a major phase of unroofing in the Early Carboniferous (360–340 Ma; Eide *et al.* 1999), and both Viola *et al.* (2016) and Ksienzyk *et al.* (2016) present Early Carboniferous (*c.* 350 Ma) faulting ages for two separate faults in western Norway (Fig. 8b). However, there is no documentation of any post-collisional extensional deformation in the foreland section of the orogen, i.e. in southeast Norway and southwest Sweden. The steep NW–SE strike of the HØDZ is also severely misoriented with regard to the dominating Devonian to Early Carboniferous NW–SE to E–W extension direction in western Norway (e.g. Fossen, 1992; Osmundsen & Andersen, 2001).

In Late Devonian to Early Carboniferous times, the southern margin of Baltica was affected by the onset of the Variscan orogeny to the south (e.g. Kalani *et al.* 2020; Fig. 8b). In the Saxo-Thuringian zone in the north of the orogen, initiation of convergence and collision is constrained between *c.* 380 and 360 Ma (Franke *et al.* 2017 and references therein). Along the southwestern margin of Baltica, this convergence was primarily expressed by significant dextral strike-slip deformation along NW–SE-striking faults and shear zones (Mazur *et al.* 2020), such as the Sorgenfrei–Tornquist zone and the HØDZ. We therefore speculate that the Late Devonian to Early Carboniferous ^{40}Ar – ^{39}Ar plateau ages of the HØDZ pseudotachylites indicate one or several reactivation events caused by far-field stresses from the Variscan Orogeny (Fig. 8b). Variscan crustal shortening is also suggested as a possible tectonic source for the slickensided fracture planes at Forsmark (Tillberg *et al.* 2020), which was interpreted as sinistral strike-slip faults. The HØDZ, in contrast, may possibly have been active as a dextral transpressive fault zone due to its NW–SE orientation with regard to the assumed N–S-oriented Variscan shortening field (Fig. 8b). Although the kinematic framework of this deformation phase in the HØDZ needs to be better constrained, the interpretation may have consequences for the understanding of the larger Sorgenfrei–Tornquist zone. The initiation of this deformation zone is commonly attributed to Late Carboniferous dextral transtension (Erlström, 2020), but the new results presented herein suggest that it could have been formed in a transpressional setting already in the Late Devonian to Early Carboniferous (Fig. 8b).

6.c.5. Permian brittle reactivation events (Fig. 8c)

The tectonomagmatic evolution of the Oslo Rift is well constrained by relative and absolute dating of its igneous and early sedimentary components (Ramberg & Larsen, 1978; Larsen *et al.* 2008a; Corfu & Larsen, 2020). Age constraints on the structures controlling the localization of rifting are, however, lacking. The only exception is a K–Ar fault gouge pseudo-plateau age of *c.* 270–260 Ma from two N–S-trending faults in the Kongsberg Ag mines west of the Oslo

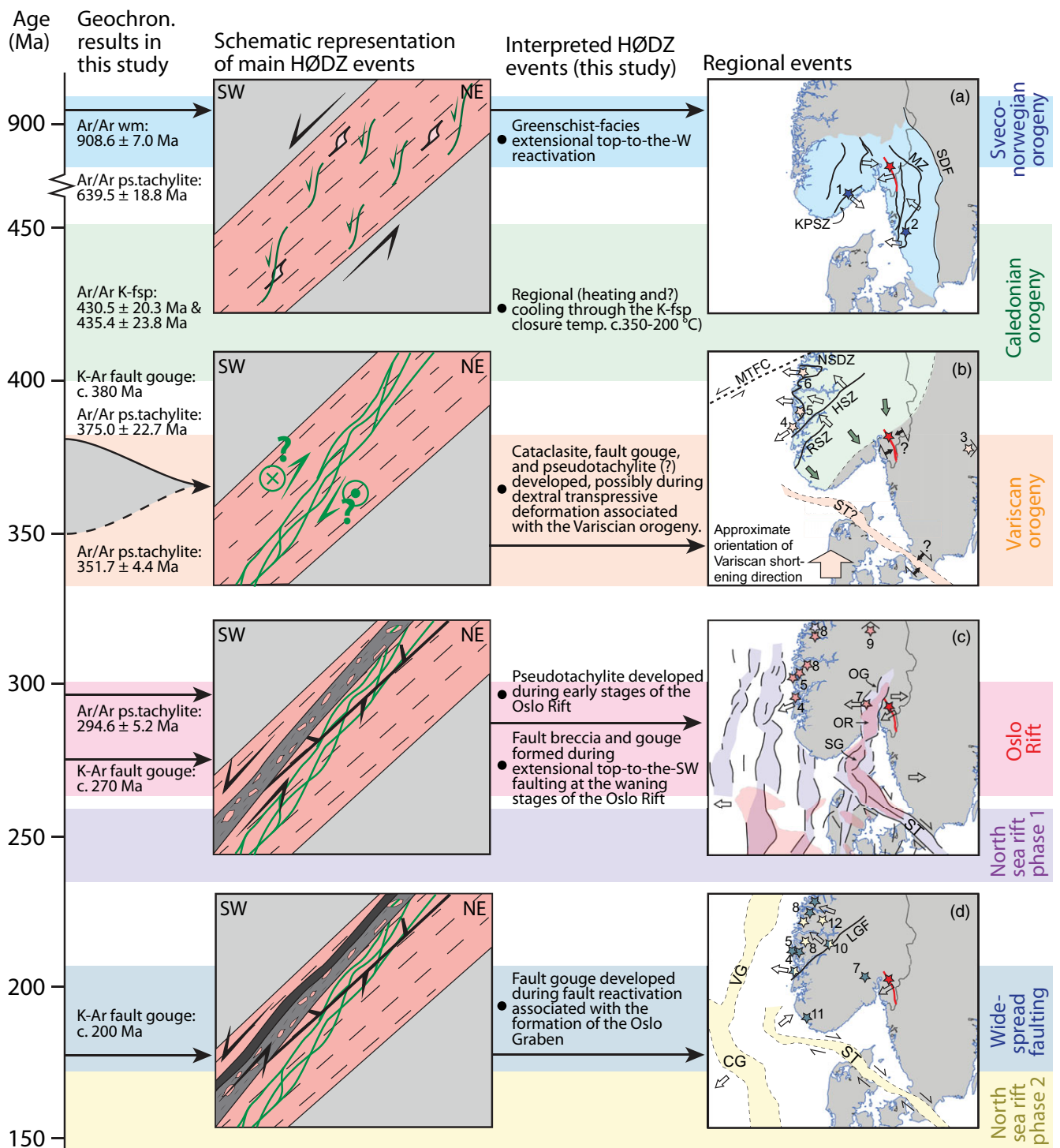


Fig. 8. (Colour online) Graphic summary of the recorded deformation events along the Hørdal–Ørje Deformation Zone and its interpreted regional context. Age data in regional events maps from 1. Mulch *et al.* (2005); 2. Viola *et al.* (2011); 3. Tillberg *et al.* (2020); 4. Viola *et al.* (2016), Scheiber & Viola (2018) and Scheiber *et al.* (2019); 5. Ksienzyk *et al.* (2016); 6. Eide *et al.* (1999); 7. Torgersen *et al.* (2015b); 8. Fossen *et al.* (2021); 9. Sherlock *et al.* (2004); 10. Tartaglia *et al.* (2020); 11. Ferstad (2017); 12. Hestnes *et al.* (2022). Offshore regional events based mostly on Kalani *et al.* (2020). Abbreviations: SDF: Scandinavian Deformation Front; MZ: Mylonite Zone; KPSZ: Kristiansand–Porsgrunn Shear Zone; ST: Sorgenfrei–Tornquist Zone; MTFC: Møre–Trøndelag Fault Complex; NSDZ: Nordfjord–Sogn Detachment Zone; HSZ: Hardangerfjord Shear Zone; RDZ: Røldal Shear Zone; OG: Oslo Graben; OR: Oslo Rift; SG: Skagerrak Graben; LGF: Lærdal Gjende Fault; VG: Viking Graben; CG: Central Graben.

Rift (Fig. 8c; Torgersen *et al.* 2015b). The *c.* 270 Ma pseudo-plateau age of the black fault gouge in the current study (BITE134; Figs 5, 7) documents that also the HØDZ, east of the rift, was reactivated at this time interval (Fig. 8c). Scarce kinematic data from these faults suggest dominating SE–NW to E–W extension, which is

in accordance with the calculated Permo–Carboniferous palaeo-stress field of the Oslo Region (Sippel *et al.* 2010). These faulting events correspond in time to the final stages of major magmatism and caldera collapses in the Oslo Rift (Larsen *et al.* 2008a; Corfu & Larsen, 2020). Some small alkaline gabbros were intruded along

N–S tectonic lineaments around 265 Ma (Neumann *et al.* 1985), which indicates that the faults also impacted on the localization of magmatism by acting as magma conduits.

The high-temperature-steps plateau age of SB009 pseudotachylite (294.6 ± 5.2 Ma; Fig. 6e) is a significant deformation age obtained in this study. It is interpreted to date the formation of pseudotachylites along the HØDZ, and its age is identical within error to the earliest recorded magmatism in the Oslo Rift (between 299 and 300 Ma; Corfu & Dahlgren, 2008; Corfu & Larsen, 2020). As such, it is the first geochronological documentation of deformation associated with the initial development of the Oslo Rift and shows that rifting was coupled with seismic activity (Fig. 8c). Curiously, the age is also identical within error to pseudotachylite ^{40}Ar – ^{39}Ar laserprobe ages from the sinistral transtensional Møre–Trøndelag Fault Complex to the north of the Oslo Rift (Fig. 8c; Sherlock *et al.* 2004).

Early–Mid Permian brittle deformation in Scandinavia is not limited to the Oslo Region. Similar faulting ages have also been documented in multiple K–Ar fault-dating studies in western Norway (Ksienzyk *et al.* 2016; Viola *et al.* 2016; Fossen *et al.* 2017; Scheiber & Viola, 2018; Scheiber *et al.* 2019), and even in northern Scotland (Kemp *et al.* 2019) and western Greenland (Rotevatn *et al.* 2018). It appears that this time interval represents an initial phase of widely distributed extension that is followed by the Late Permian to Early Triassic localized development of the northern North Sea rift and its counterpart in the Skagerrak graben (Fig. 8c; Gabrielsen *et al.* 1990; Fossen *et al.* 2021). At a larger scale, the Early–Mid Permian marks a time interval where numerous rift systems developed throughout the newly assembled Pangaea supercontinent, eventually leading to the formation of the Neo-Tethys Ocean (e.g. Frizon de Lamotte *et al.* 2015).

6.c.6. Latest Triassic – Earliest Jurassic brittle reactivation (Fig. 8d)

The last datable activity along the HØDZ documented in our study is constrained by the overlapping ages of the finest size fraction in all three fault gouges at *c.* 200 Ma (Figs 7, 8d). This reactivation event must have been considerable since it involved authigenic mineral growth in all the HØDZ fault gouges. This argument is echoed on a larger scale by the fact that most of the dated fault gouges so far in southern Norway constrain fault activity around 200–150 Ma (Ksienzyk *et al.* 2016; Viola *et al.* 2016; Scheiber *et al.* 2019; Tartaglia *et al.* 2020; Fossen *et al.* 2021; Hestnes *et al.* 2022), also including the Kongsberg Ag-mines faults at *c.* 200 Ma (Torgersen *et al.* 2015b). Similar to the Early–Mid Permian faulting phase, this phase of widespread brittle deformation also predates major rifting offshore (North Sea rift phase 2; Fig. 8d), leading Fossen *et al.* (2021) to speculate whether this behaviour is a typical trait of continental rifting. It should be noted that the initiation of this Early Jurassic faulting phase around 200 Ma matches exactly with the emplacement of the Central Atlantic magmatic province (CAMP; Marzoli *et al.* 2018 and references therein), which marks the start of the true disintegration of supercontinent Pangaea, according to Frizon de Lamotte *et al.* (2015).

6.d. Fault localization and reactivation in plastic shear zones

The regional shear zones in the Sveconorwegian basement of southern Norway and Sweden are likely of lithospheric scale (e.g. Viola *et al.* 2011; Bingen *et al.* 2021), representing deformation zones that separate lithotectonic units with distinct geological histories. Important stages in the structural development of these

deformation zones are preserved in the variety of partly overprinting deformation rocks that reveal shifting pressure- and temperature conditions and variation in stress field orientations. Once established, such structures tend to absorb repeated strain episodes independently of shifting *P*–*T* conditions and strain intensity (Watterson, 1975; Sibson, 1977; Nur, 1982; Gabrielsen, 1984; Gabrielsen & Braathen, 2014). The deformation geochronology presented herein shows that brittle deformation (i.e. Himdalen Fault) localized into and exploited the pre-existing Ørje Shear Zone throughout several distinct tectonic episodes (Fig. 8). This structural reactivation demonstrates that pre-existing lithospheric-scale zones of weakness may be preferentially reactivated whenever they are in a (semi-)favourable orientation in relation to the principal stress configuration.

Whereas the mechanisms that control repeated reactivation of brittle faults have been much studied (e.g. Sibson, 1985; Rutter *et al.* 2001; Collettini *et al.* 2019), less is understood about the mechanisms that control the initiation of brittle deformation along pre-existing plastic shear zones. One hypothesis is that semi-continuous deformation across the brittle–plastic transition, such as in many large extensional detachment zones (e.g. Norton, 1986; Fossen, 1992; Andersen, 1998; Braathen *et al.* 2004), is required. However, the current study suggests that brittle deformation, represented by cataclite, pseudotachylite and fault gouge, postdates the mylonitic fabric by more than 500 Ma (Fig. 8). Although we cannot exclude the possibility that minor cataclastic deformation was cogenetic with mylonitic shearing, it seems improbable that this should have had a major control on the brittle rheology of the shear zone.

Instead, we would highlight the fact that the brittle deformational rocks in HØDZ are almost perfectly parallel with the mylonitic fabric (Figs. 1–4), which leads us to suggest that the *c.* 908 Ma Ørje Shear Zone fabric was a lithospheric-scale mechanical anisotropy at the time of initial brittle deformation (*c.* 380–350 Ma; Fig. 8). The anisotropy was defined not only by quartz–felspathic segregation bands and parallel-oriented phyllosilicate planes (e.g. Fig. 3c–d), but also by alternating parallel-oriented phyllosilicate-rich lithologies such as phyllonites and sheared mafic dikes (Fig. 2). The importance of such mechanical anisotropies in controlling localization of brittle strain in plastic shear zones has been shown in field studies (e.g. Wehrens *et al.* 2017), analogue experiments (e.g. Samsu *et al.* 2021), rock deformation experiments (e.g. Paterson & Wong, 2015) and numerical modelling (e.g. Vauchez *et al.* 1998; Naliboff *et al.* 2017). Wehrens *et al.* (2017) describe the phyllosilicate content and its spatial distribution as crucial for controlling the distribution of strain. This is in accordance with studies of phyllosilicate frictional properties, which are shown to be strongly dependent on their organization into throughgoing foliation planes (e.g. Collettini *et al.* 2009; Tesei *et al.* 2012; Haines *et al.* 2013). We therefore suggest that mechanical anisotropy of mylonitic fabrics is produced by parallel-oriented throughgoing phyllosilicate planes that can weaken the frictional strength of crustal-scale plastic shear zones on very long timescales. Crustal-scale shear zones may therefore impose a large-scale mechanical anisotropy on the strength of the crust, making them the most probable loci for accommodating subsequent brittle strain increments.

7. Conclusions

This structural–geochronological study of the Himdalen–Ørje Deformation Zone (HØDZ) uncovers the potentially long-lived,

yet punctuated, structural evolution of geologically old, large-scale deformation zones. The study shows the importance of combining different geochronological methods with structural analysis and mineralogical constraints to characterize the evolution of such deformation zones. The main conclusions of this work are:

- The HØDZ comprises a large range of deformation rocks from mylonite to fault gouge that reflects repeated structural reactivations during changing pressure-, temperature- and stress conditions.
- The deformation zone was formed as a top-to-the-E compressional shear zone during the Mesoproterozoic Sveconorwegian orogeny, but the oldest geochronological data obtained in this study date late-Sveconorwegian, greenschist-facies top-to-the-W extensional reactivation at 908.6 ± 7.0 Ma (^{40}Ar – ^{39}Ar white mica plateau age).
- The first phase of brittle deformation is constrained between c. 380 Ma and c. 350 Ma by ^{40}Ar – ^{39}Ar plateau ages of pseudotachylite veins and K–Ar ages of the coarsest size fractions in two fault gouges. We suggest that this event was caused by far-field stresses of the Variscan orogeny to the south.
- Major structural reactivation of the HØDZ occurred during the development of the Permian Oslo Rift, as documented by K–Ar fault gouge dating (c. 270 Ma) and a ^{40}Ar – ^{39}Ar pseudotachylite plateau age (294.6 ± 5.2 Ma). We interpret the latter to document seismic activity during the initiation of rift magmatism.
- The last datable reactivation of the HØDZ was at c. 200 Ma, as recorded by K–Ar fault gouge dating. The age is similar to those derived from multiple other K–Ar fault-dating studies in southern Norway and testifies to a time interval of extensive, widespread overall E–W extension that predates major localized Jurassic–Cretaceous rifting offshore.
- We have shown that it is possible to obtain geologically significant K–Ar ages from several generations of syn-kinematic authigenic illite within the same fault gouge if careful field sampling and structural characterization is combined with detailed mineralogical characterization, including illite crystallinity analysis.
- We suggest that the main factor controlling the initiation of brittle deformation along pre-existing plastic shear zones is mechanical anisotropy defined by the presence of parallel-oriented, interconnected phyllosilicate foliation planes within the mylonitic fabric.

Supplementary material. To view supplementary material for this article, please visit <https://doi.org/10.1017/S0016756822000966>.

Acknowledgements. Jussi Mattila and Sam Haines are greatly thanked for their thorough and honest reviews that helped improve the quality of the article. We thank Kjetil Indrevær for initiating the collaboration, Alvar Braathen for commenting on the work and Anna Ksienzyk for sharing her national compilation of K–Ar fault gouge data. Ruikai Xie is thanked for careful K analysis.

Conflicts of interest. None.

References

- Ahlin S, Hegardt EA and Cornell D (2006) Nature and stratigraphic position of the 1614 Ma Delsjön augen granite-gneiss in the Median Segment of south-west Sweden. *GFF* **128**, 21–32. doi: [10.1080/11035890601281021](https://doi.org/10.1080/11035890601281021).
- Aldega L, Viola G, Casas-Sainz A, Marcén M, Román-Berdiel T and van der Lelij R (2019) Unraveling multiple thermotectonic events accommodated by crustal-scale faults in Northern Iberia, Spain: insights from K–Ar dating of clay gouges. *Tectonics* **38**, 3629–51. doi: [10.1029/2019TC005585](https://doi.org/10.1029/2019TC005585).
- Andersen T (2005) Terrane analysis, regional nomenclature and crustal evolution in the Southwest Scandinavian Domain of the Fennoscandian Shield. *GFF* **127**, 159–68. doi: [10.1080/11035890501272159](https://doi.org/10.1080/11035890501272159).
- Andersen T and Grorud HF (1998) Age and lead isotope systematics of uranium-enriched cobalt mineralization in the Modum complex, South Norway: implications for Precambrian crustal evolution in the SW part of the Baltic Shield. *Precambrian Research* **91**, 419–32. doi: [10.1016/S0301-9268\(98\)00061-8](https://doi.org/10.1016/S0301-9268(98)00061-8).
- Andersen TB (1998) Extensional tectonics in the Caledonides of southern Norway, an overview. *Tectonophysics* **285**, 333–51. doi: [10.1016/S0040-1951\(97\)00277-1](https://doi.org/10.1016/S0040-1951(97)00277-1).
- Andersen TB and Jamtveit B (1990) Uplift of deep crust during orogenic extensional collapse: a model based on field studies in the Sogn-Sunnfjord Region of western Norway. *Tectonics* **9**, 1097–1111. doi: [10.1029/TC009i005p01097](https://doi.org/10.1029/TC009i005p01097).
- Backeberg NR, Rowe CD and Barshi N (2016) Alteration-weakening leading to localized deformation in a damage aureole adjacent to a dormant shear zone. *Journal of Structural Geology* **90**, 144–56. doi: [10.1016/j.jsg.2016.07.008](https://doi.org/10.1016/j.jsg.2016.07.008).
- Berthelsen A (1980) Towards a palinspastic tectonic analysis of the Baltic Shield. In *Geology of Europe from Precambrian to Post-Hercynian Sedimentary Basins* (eds J Cogne and M Slansky), pp. 5–21. Mémoires du B.R.G.M., 6th Colloquium of the International Geological Congress, Paris.
- Bingen B, Birkeland A, Nordgulen O and Sigmond EMO (2001) Correlation of supracrustal sequences and origin of terranes in the Sveconorwegian orogen of SW Scandinavia: SIMS data on zircon in clastic metasediments. *Precambrian Research* **108**, 293–318. doi: [10.1016/S0301-9268\(01\)00133-4](https://doi.org/10.1016/S0301-9268(01)00133-4).
- Bingen B, Davis WJ, Hamilton MA, Engvik AK, Stein HJ, Skar O and Nordgulen O (2008a) Geochronology of high-grade metamorphism in the Sveconorwegian belt, S. Norway: U–Pb, Th–Pb and Re–Os data. *Norwegian Journal of Geology* **88**, 13–42.
- Bingen B, Nordgulen O and Viola G (2008b) A four-phase model for the Sveconorwegian orogeny, SW Scandinavia. *Norwegian Journal of Geology* **88**, 43–72.
- Bingen B and Viola G (2018) The early-Sveconorwegian orogeny in southern Norway: tectonic model involving delamination of the sub-continental lithospheric mantle. *Precambrian Research* **313**, 170–204. doi: [10.1016/j.precamres.2018.05.025](https://doi.org/10.1016/j.precamres.2018.05.025).
- Bingen B, Viola G, Möller C, Vander Auwera J, Laurent A and Yi K (2021) The Sveconorwegian orogeny. *Gondwana Research* **90**, 273–313. doi: [10.1016/j.gr.2020.10.014](https://doi.org/10.1016/j.gr.2020.10.014).
- Bolognesi F and Bistacchi A (2016) Weakness and mechanical anisotropy of phyllosilicate-rich cataclases developed after mylonites of a low-angle normal fault (Simplon Line, Western Alps). *Journal of Structural Geology* **83**, 1–12. doi: [10.1016/j.jsg.2015.11.009](https://doi.org/10.1016/j.jsg.2015.11.009).
- Braathen A, Osmundsen PT and Gabrielsen RH (2004) Dynamic development of fault rocks in a crustal-scale detachment: an example from western Norway. *Tectonics* **23**. doi: [10.1029/2003TC001558](https://doi.org/10.1029/2003TC001558).
- Braathen A, Osmundsen PT, Maher H and Ganerød M (2018) The Keisarhjelmen detachment records Silurian–Devonian extensional collapse in Northern Svalbard. *Terra Nova* **30**, 34–9. doi: [10.1111/ter.12305](https://doi.org/10.1111/ter.12305).
- Bruton DL, Gabrielsen RH and Larsen BT (2010) The Caledonides of the Oslo Region, Norway: stratigraphy and structural elements. *Norwegian Journal of Geology/Norsk Geologisk Forening* **90**, 93–121.
- Bugge A (1936) Kongsberg-Bamble formasjonen. *Norges Geologiske Undersøkelse – NGU* **146**, 1–117.
- Charbit S, Guillou H and Turpin L (1998) Cross calibration of K–Ar standard minerals using an unspiked Ar measurement technique. *Chemical Geology* **150**, 147–59.
- Clauer N and Chaudhuri S (1995) *Clays in Crustal Environments: Isotope Dating and Tracing*. Berlin and Heidelberg: Springer-Verlag.
- Collettini C, Niemeijer A, Viti C and Marone C (2009) Fault zone fabric and fault weakness. *Nature* **462**, 907–10. doi: [10.1038/nature08585](https://doi.org/10.1038/nature08585).
- Collettini C, Tesi T, Scuderi MM, Carpenter BM and Viti C (2019) Beyond Byerlee friction: weak faults and implications for slip behavior. *Earth and Planetary Science Letters* **519**, 245–63. doi: [10.1016/j.epsl.2019.05.011](https://doi.org/10.1016/j.epsl.2019.05.011).

- Corfu F, Andersen TB and Gasser D** (2014) The Scandinavian Caledonides: main features, conceptual advances and critical questions. In *New Perspectives on the Caledonides of Scandinavia and Related Areas* (eds F Corfu, D Gasser and DM Chew), pp. 9–43. Geological Society of London, Special Publication no. 390. doi: [10.1144/sp390.25](https://doi.org/10.1144/sp390.25).
- Corfu F and Dahlgren S** (2008) Perovskite U–Pb ages and the Pb isotopic composition of alkaline volcanism initiating the Permo–Carboniferous Oslo Rift. *Earth and Planetary Science Letters* **265**, 256–69. doi: [10.1016/j.epsl.2007.10.019](https://doi.org/10.1016/j.epsl.2007.10.019).
- Corfu F and Larsen BT** (2020) U–Pb systematics in volcanic and plutonic rocks of the Krokskogen area: resolving a 40 million years long evolution in the Oslo Rift. *Lithos* **376–377**, 105755. doi: [10.1016/j.lithos.2020.105755](https://doi.org/10.1016/j.lithos.2020.105755).
- Crider JG** (2015) The initiation of brittle faults in crystalline rock. *Journal of Structural Geology* **77**, 159–74. doi: [10.1016/j.jsg.2015.05.001](https://doi.org/10.1016/j.jsg.2015.05.001).
- Davis GA, Darby BJ, Yadong Z and Spell TL** (2002) Geometric and temporal evolution of an extensional detachment fault, Hohhot metamorphic core complex, Inner Mongolia, China. *Geology* **30**, 1003–6. doi: [10.1130/0091-7613\(2002\)030<1003:Gateoa>2.0.Co;2](https://doi.org/10.1130/0091-7613(2002)030<1003:Gateoa>2.0.Co;2).
- Di Vincenzo G, Rocchi S, Rossetti F and Storti F** (2004) ⁴⁰Ar–³⁹Ar dating of pseudotachylytes: the effect of clast-hosted extraneous argon in Cenozoic fault-generated friction melts from the West Antarctic Rift System. *Earth and Planetary Science Letters* **223**, 349–64. doi: [10.1016/j.epsl.2004.04.042](https://doi.org/10.1016/j.epsl.2004.04.042).
- Eide EA, Torsvik TH and Andersen TB** (1997) Absolute dating of brittle fault movements: late Permian and late Jurassic extensional fault breccias in western Norway. *Terra Nova* **9**, 135–9. doi: [10.1046/j.1365-3121.1997.d01-21.x](https://doi.org/10.1046/j.1365-3121.1997.d01-21.x).
- Eide EA, Torsvik TH, Andersen TB and Arnaud NO** (1999) Early Carboniferous unroofing in Western Norway: a tale of alkali feldspar thermochronology. *The Journal of Geology* **107**, 353–74. doi: [10.1086/314351](https://doi.org/10.1086/314351).
- Erlström M** (2020) Carboniferous–Neogene tectonic evolution of the Fennoscandian transition zone, southern Sweden. *Geological Society of London, Memoirs* **50**, 603–20. doi: [10.1144/m50-2016-25](https://doi.org/10.1144/m50-2016-25).
- Ferreira JM, Bezerra FHR, Sousa MO, do Nascimento AF, Sá JM and França GS** (2008) The role of Precambrian mylonitic belts and present-day stress field in the coseismic reactivation of the Pernambuco lineament, Brazil. *Tectonophysics* **456**, 111–26. doi: [10.1016/j.tecto.2008.01.009](https://doi.org/10.1016/j.tecto.2008.01.009).
- Ferstad A-LK** (2017) Multiscalar structural study of the brittle deformation history in the Åna-Sira anorthosite massif, Rogaland, Southwestern Norway. Trondheim: Department of Geoscience and Petroleum, Norwegian University of Science and Technology. <https://ntnuopen.ntnu.no/ntnu-xmlui/handle/11250/2447392?locale-attribute=en>
- Fossen H** (1992) The role of extensional tectonics in the Caledonides of south Norway. *Journal of Structural Geology* **14**, 1033–46. doi: [10.1016/0191-8141\(92\)90034-T](https://doi.org/10.1016/0191-8141(92)90034-T).
- Fossen H, Khani HF, Faleide JI, Ksienzyk AK and Dunlap WJ** (2017) Post-Caledonian extension in the West Norway–northern North Sea region: the role of structural inheritance. In *The Geometry and Growth of Natural Faults* (ed. D Childs), pp. 465–86. Geological Society of London, Special Publication no. 439. doi: [10.1144/SP439.6](https://doi.org/10.1144/SP439.6).
- Fossen H, Ksienzyk AK, Rotevatn A, Bauck MS and Wemmer K** (2021) From widespread faulting to localised rifting: evidence from K–Ar fault gouge dates from the Norwegian North Sea rift shoulder. *Basin Research* **33**, 1934–53. doi: [10.1111/bre.12541](https://doi.org/10.1111/bre.12541).
- Fossen H** (2010) Extensional tectonics in the North Atlantic Caledonides: a regional view. In *Continental Tectonics and Mountain Building: The Legacy of Peach and Home* (eds RD Law, RWH Butler, RE Holdsworth, M Krabbendam & RA Strachan), pp. 767–93. Geological Society of London, Special Publication no. 335. doi: [10.1144/sp335.31](https://doi.org/10.1144/sp335.31).
- Fossen H, Mangerud G, Hesthammer J, Bugge T and Gabrielsen RH** (1997) The Bjorøy Formation: a newly discovered occurrence of Jurassic sediments in the Bergen Arc system. *Norsk Geologisk Tidsskrift* **77**, 269–87.
- Franke W, Cocks LRM and Torsvik TH** (2017) The Palaeozoic Variscan oceans revisited. *Gondwana Research* **48**, 257–84. doi: [10.1016/j.gr.2017.03.005](https://doi.org/10.1016/j.gr.2017.03.005).
- Frizon de Lamotte D, Fourdan B, Leleu S, Leparmentier F and de Clarens P** (2015) Style of rifting and the stages of Pangea breakup. *Tectonics* **34**, 1009–29. doi: [10.1002/2014TC003760](https://doi.org/10.1002/2014TC003760).
- Fuhrmann U, Lippolt H and Hess J** (1987) HD-B1 biotite reference material for K–Ar chronometry. *Chemical Geology* **66**, 41–51.
- Gaál G and Gorbatschev R** (1987) An outline of the Precambrian evolution of the Baltic Shield. *Precambrian Research* **35**, 15–52.
- Gabrielsen RH, Færseth RB, Steel RJ and Kløvjan OS** (1990) Architectural styles of basin fill in the northern Viking Graben. In *Evolution of the North Sea Rifts* (eds D Blundell and A Gibbs), pp. 158–179. Oxford, UK: Oxford Press.
- Gabrielsen RH** (1984) Long-lived fault zones and their influence on the tectonic development of the southwestern Barents Sea. *Journal of the Geological Society* **141**, 651–62. doi: [10.1144/gsjgs.141.4.0651](https://doi.org/10.1144/gsjgs.141.4.0651).
- Gabrielsen RH and Braathen A** (2014) Models of fracture lineaments: joint swarms, fracture corridors and faults in crystalline rocks, and their genetic relations. *Tectonophysics* **628**, 26–44. doi: [10.1016/j.tecto.2014.04.022](https://doi.org/10.1016/j.tecto.2014.04.022).
- Gabrielsen RH, Nystuen JP and Olesen O** (2018) Fault distribution in the Precambrian basement of South Norway. *Journal of Structural Geology* **108**, 269–89. doi: [10.1016/j.jsg.2017.06.006](https://doi.org/10.1016/j.jsg.2017.06.006).
- Gabrielsen RH, Olesen O, Braathen A, Faleide JI, Baranwal VC and Lindholm C** (2019) The Listafjorden–Drangedal Fault Complex of the Agder–Telemark Lineament Zone, southern Norway: a structural analysis based on remote sensing and potential field data. *GFF* **141**, 200–15. doi: [10.1080/11035897.2019.1624978](https://doi.org/10.1080/11035897.2019.1624978).
- Gabrielsen RH and Ramberg IB** (1979) Fracture patterns in Norway from LANDSAT imagery: results and potential use. In *Proceedings, Norwegian Sea Symposium*, pp. 1–28. Tromsø: Norwegian Petroleum Society.
- Ganerød GV, Braathen A and Willemoes-Wissing B** (2008) Predictive permeability model of extensional faults in crystalline and metamorphic rocks: verification by pre-grouting in two sub-sea tunnels, Norway. *Journal of Structural Geology* **30**, 993–1004. doi: [10.1016/j.jsg.2008.04.001](https://doi.org/10.1016/j.jsg.2008.04.001).
- Gorbatschev R** (1988) Sveconorwegian thrusting in southwestern Sweden. *Geologiska Föreningen i Stockholm Förhandlingar* **110**, 392–7.
- Grathoff GH and Moore DM** (1996) Illite polytype quantification using WILDFIRE© calculated X-ray diffraction patterns. *Clays and Clay Minerals* **44**, 835–42.
- Gundlach-Graham A, Garofalo PS, Schwarz G, Redi D and Günther D** (2018) High-resolution, quantitative element imaging of an upper crust, low-angle cataclasis (Zuccale Fault, Northern Apennines) by laser ablation ICP time-of-flight mass spectrometry. *Geostandards and Geoanalytical Research* **42**, 559–74. doi: [10.1111/ggr.12233](https://doi.org/10.1111/ggr.12233).
- Hageskov B** (1980) The Sveconorwegian structures of the Norwegian part of the Kongsberg-Bamble-Østfold segment. *Geologiska Föreningen i Stockholm Förhandlingar* **102**, 150–5.
- Haines S, Marone C and Saffer D** (2014) Frictional properties of low-angle normal fault gouges and implications for low-angle normal fault slip. *Earth and Planetary Science Letters* **408**, 57–65. doi: [10.1016/j.epsl.2014.09.034](https://doi.org/10.1016/j.epsl.2014.09.034).
- Haines SH, Kaproth B, Marone C, Saffer D and van der Pluijm B** (2013) Shear zones in clay-rich fault gouge: a laboratory study of fabric development and evolution. *Journal of Structural Geology* **51**, 206–25. doi: [10.1016/j.jsg.2013.01.002](https://doi.org/10.1016/j.jsg.2013.01.002).
- Haines SH and van der Pluijm BA** (2008) Clay quantification and Ar–Ar dating of synthetic and natural gouge: application to the Miocene Sierra Mazatan detachment fault, Sonora, Mexico. *Journal of Structural Geology* **30**, 525–38. doi: [10.1016/j.jsg.2007.11.012](https://doi.org/10.1016/j.jsg.2007.11.012).
- Haines SH and van der Pluijm BA** (2012) Patterns of mineral transformations in clay gouge, with examples from low-angle normal fault rocks in the western USA. *Journal of Structural Geology* **43**, 2–32. doi: [10.1016/j.jsg.2012.05.004](https://doi.org/10.1016/j.jsg.2012.05.004).
- Hałas S and Wójtowicz A** (2014) Propagation of error formulas for K/Ar dating method. *Geochronometria* **41**, 202–6.
- Heaman LM and Smalley PC** (1994) A U–Pb study of the Morkheia Complex and associated gneisses, southern Norway: implications for disturbed Rb–Sr systems and for the temporal evolution of Mesoproterozoic magmatism in Laurentia. *Geochimica et Cosmochimica Acta* **58**, 1899–911. doi: [10.1016/0016-7037\(94\)90423-5](https://doi.org/10.1016/0016-7037(94)90423-5).
- Heier KS** (1962) Trace elements in feldspars – a review. *Norsk Geologisk Tidsskrift* **42**, 415–54.

- Hestnes Å, Gasser D, Scheiber T, Jacobs J, van der Lelij R, Schönenberger J and Ksienzyk AK (2022) The brittle evolution of Western Norway: a space-time model based on fault mineralizations, K–Ar fault gouge dating and paleostress analysis. *Journal of Structural Geology* **160**, 104621. doi: [10.1016/j.jsg.2022.104621](https://doi.org/10.1016/j.jsg.2022.104621).
- Högdahl K, Gromet LP and Broman C (2001) Low P–T Caledonian resetting of U-rich Paleoproterozoic zircons, central Sweden. *American Mineralogist* **86**, 534–46. doi: [10.2138/am-2001-0416](https://doi.org/10.2138/am-2001-0416).
- Holdsworth RE, Butler CA and Roberts AM (1997) The recognition of reactivation during continental deformation. *Journal of the Geological Society* **154**, 73–8. doi: [10.1144/gsjgs.154.1.0073](https://doi.org/10.1144/gsjgs.154.1.0073).
- Hueck M, Wemmer K, Ksienzyk AK, Kuehn R and Vogel N (2022) Potential, premises, and pitfalls of interpreting illite argon dates: a case study from the German Variscides. *Earth-Science Reviews* **232**, 104133. doi: [10.1016/j.earscirev.2022.104133](https://doi.org/10.1016/j.earscirev.2022.104133).
- Jefferies SP, Holdsworth RE, Wibberley CAJ, Shimamoto T, Spiers CJ, Niemeijer AR and Lloyd GE (2006) The nature and importance of phyllonite development in crustal-scale fault cores: an example from the Median Tectonic Line, Japan. *Journal of Structural Geology* **28**, 220–35. doi: [10.1016/j.jsg.2005.10.008](https://doi.org/10.1016/j.jsg.2005.10.008).
- Johansson L and Johansson Å (1993) U–Pb age of titanite in the Mylonite Zone, southwestern Sweden. *Geologiska Föreningen i Stockholm Förhandlingar* **115**, 1–7.
- Kalani M, Faleide JJ and Gabrielsen RH (2020) Paleozoic–Mesozoic tectono-sedimentary evolution and magmatism of the Egersund Basin area, Norwegian central North Sea. *Marine and Petroleum Geology* **122**, 104642. doi: [10.1016/j.marpetgeo.2020.104642](https://doi.org/10.1016/j.marpetgeo.2020.104642).
- Kemp SJ, Gillespie MR, Leslie GA, Zwingmann H and Campbell SDG (2019) Clay mineral dating of displacement on the Sronlairig Fault: implications for Mesozoic and Cenozoic tectonic evolution in northern Scotland. *Clay Minerals* **54**, 181–96. doi: [10.1180/clm.2019.25](https://doi.org/10.1180/clm.2019.25).
- Kirkpatrick JD and Rowe CD (2013) Disappearing ink: how pseudotachylites are lost from the rock record. *Journal of Structural Geology* **52**, 183–98. doi: [10.1016/j.jsg.2013.03.003](https://doi.org/10.1016/j.jsg.2013.03.003).
- Kjøll HJ (2020) Late Neoproterozoic basin evolution of the magma-rich Iapetus margin of Baltica. *Norwegian Journal of Geology* **100**, 202005. doi: [10.17850/njg100-1-6](https://doi.org/10.17850/njg100-1-6).
- Ksienzyk AK, Wemmer K, Jacobs J, Fossen H, Schomberg AC, Süßenberger A, Lünsdorf NK and Bastesen E (2016) Post-Caledonian brittle deformation in the Bergen area, West Norway: results from K–Ar illite fault gouge dating. *Norwegian Journal of Geology* **96**, 275–99.
- Kumpulainen R and Nystuen J (1985) Late Proterozoic basin evolution and sedimentation in the westernmost part of Baltoscandia. In *The Caledonide Orogen – Scandinavia and Related Areas* (eds D Gee and B Sturt), pp. 213–45. Chichester: John Wiley & Sons Ltd.
- Larsen BT, Olausen S, Sundvoll B and Heeremans M (2008a) The Permo-Carboniferous Oslo Rift through six stages and 65 million years. *Episodes* **31**, 52–8. doi: [10.18814/epiugs/2008/v31i1/008](https://doi.org/10.18814/epiugs/2008/v31i1/008).
- Larsen BT, Olausen S, Sundvoll B and Heeremans M (2008b) Volcanoes and faulting in an arid climate: the Oslo Rift and North Sea in the Carboniferous and Permian. In *The Making of a Land: Geology of Norway* (eds IB Ramberg, I Bryhni and A Nøttvedt), pp. 260–303. Trondheim: Geological Society of Norway.
- Lee J-Y, Marti K, Severinghaus JP, Kawamura K, Yoo H-S, Lee JB and Kim JS (2006) A redetermination of the isotopic abundances of atmospheric Ar. *Geochimica et Cosmochimica Acta* **70**, 4507–12.
- Margerie E and Heim A (1888) *Les dislocations de l'écorce terrestre. Die Dislocationen der Erdrinde. Essai de définition et de nomenclature. Versuch einer Definition und Bezeichnung*. Zürich: J. Wurster & Comp.
- Marzoli A, Callegaro S, Dal Corso J, Davies JHFL, Chiaradia M, Youbi N, Bertrand H, Reisberg L, Merle R and Jourdan F (2018) The Central Atlantic Magmatic Province (CAMP): a Review. In *The Late Triassic World: Earth in a Time of Transition* (ed LH Tanner), pp. 91–125. Cham: Springer International Publishing. doi: [10.1007/978-3-319-68009-5_4](https://doi.org/10.1007/978-3-319-68009-5_4).
- Mazur S, Aleksandrowski P, Gągała Ł, Krzywiac P, Żaba J, Gaidzik K and Sikora R (2020) Late Palaeozoic strike-slip tectonics versus oroclinal bending at the SW outskirts of Baltica: case of the Variscan belt's eastern end in Poland. *International Journal of Earth Sciences* **109**, 1133–60. doi: [10.1007/s00531-019-01814-7](https://doi.org/10.1007/s00531-019-01814-7).
- McDougall I and Wellman P (2011) Calibration of GA1550 biotite standard for K/Ar and $^{40}\text{Ar}/^{39}\text{Ar}$ dating. *Chemical Geology* **280**, 19–25.
- Möller C and Andersson J (2018) Metamorphic zoning and behaviour of an underthrusting continental plate. *Journal of Metamorphic Geology* **36**, 567–89.
- Möller C, Andersson J, Dyck B and Lundin IA (2015) Exhumation of an eclogite terrane as a hot migmatitic nappe, Sveconorwegian orogen. *Lithos* **226**, 147–68.
- Morley CK, Haranya C, Phoosongsee W, Pongwapee S, Kornawan A and Wonganan N (2004) Activation of rift oblique and rift parallel pre-existing fabrics during extension and their effect on deformation style: examples from the rifts of Thailand. *Journal of Structural Geology* **26**, 1803–29. doi: [10.1016/j.jsg.2004.02.014](https://doi.org/10.1016/j.jsg.2004.02.014).
- Mottram CM, Kellett DA, Barresi T, Zwingmann H, Friend M, Todd A and Percival JB (2020) Syncing fault rock clocks: direct comparison of U–Pb carbonate and K–Ar illite fault dating methods. *Geology* **48**, 1179–83. doi: [10.1130/G47778.1](https://doi.org/10.1130/G47778.1).
- Mulch A, Cosca MA, Andresen A and Fiebig J (2005) Time scales of deformation and exhumation in extensional detachment systems determined by high-spatial resolution in situ UV-laser $^{40}\text{Ar}/^{39}\text{Ar}$ dating. *Earth and Planetary Science Letters* **233**, 375–90.
- Munz IA, Wayne D and Austrheim H (1994) Retrograde fluid infiltration in the high-grade modum complex South Norway: evidence for age, source and REE mobility. *Contributions to Mineralogy and Petrology* **116**, 32–46.
- Naliboff JB, Buitter SJH, Péron-Pinvidic G, Osmundsen PT and Tetreault J (2017) Complex fault interaction controls continental rifting. *Nature Communications* **8**, 1179. doi: [10.1038/s41467-017-00904-x](https://doi.org/10.1038/s41467-017-00904-x).
- Neumann E-R, Larsen BT and Sundvoll B (1985) Compositional variations among gabbroic intrusions in the Oslo rift. *Lithos* **18**, 35–59. doi: [10.1016/0024-4937\(85\)90005-2](https://doi.org/10.1016/0024-4937(85)90005-2).
- Nordbäck N, Mattila J, Zwingmann H and Viola G (2022) Precambrian fault reactivation revealed by structural and K–Ar geochronological data from the spent nuclear fuel repository in Olkiluoto, southwestern Finland. *Tectonophysics* **824**, 229208. doi: [10.1016/j.tecto.2022.229208](https://doi.org/10.1016/j.tecto.2022.229208).
- Norges Geologiske Undersøkelse (2021) 1:250 000 harmonised bedrock map database. https://geo.ngu.no/kart/common_mobil?_kart/berggrunn_mobil/_lang=eng:map=9
- Norton M (1986) Late Caledonide extension in western Norway: a response to extreme crustal thickening. *Tectonics* **5**, 195–204.
- Nur A (1982) The origin of tensile fracture lineaments. *Journal of Structural Geology* **4**, 31–40. doi: [10.1016/0191-8141\(82\)90004-9](https://doi.org/10.1016/0191-8141(82)90004-9).
- O'Hanlon JF (2005) *A User's Guide to Vacuum Technology*. Chichester: John Wiley & Sons.
- Olausen S, Larsen BT and Steel R (1994) The Upper Carboniferous–Permian Oslo Rift: basin fill in relation to tectonic development. In *Pangea: Global Environments and Resources* (ed. AF Embry), pp. 175–197. Calgary: Canadian Society of Petroleum Geology.
- Osagiede EE, Rotevatn A, Gawthorpe R, Kristensen TB, Jackson CAL and Marsh N (2020) Pre-existing intra-basement shear zones influence growth and geometry of non-colinear normal faults, western Utsira High–Heimdals Terrace, North Sea. *Journal of Structural Geology* **130**, 103908. doi: [10.1016/j.jsg.2019.103908](https://doi.org/10.1016/j.jsg.2019.103908).
- Osmundsen P and Andersen T (2001) The middle Devonian basins of western Norway: sedimentary response to large-scale transensional tectonics? *Tectonophysics* **332**, 51–68.
- Osmundsen PT, Eide EA, Haabesland NE, Roberts D, Andersen TB, Kendrick M, Bingen B, Braathen A and Redfield TF (2006) Kinematics of the Høybakken detachment zone and the Møre-Trøndelag Fault Complex, central Norway. *Journal of the Geological Society* **163**, 303–18.
- Osmundsen PT and Péron-Pinvidic G (2018) Crustal-scale fault interaction at rifted margins and the formation of domain-bounding breakaway complexes: insights from offshore Norway. *Tectonics* **37**, 935–64. doi: [10.1002/2017TC004792](https://doi.org/10.1002/2017TC004792).
- Osmundsen PT, Péron-Pinvidic G and Bunkholt H (2021) Rifting of collapsed orogens: successive incision of continental crust in the proximal

- margin offshore Norway. *Tectonics* **40**, e2020TC006283. doi: [10.1029/2020TC006283](https://doi.org/10.1029/2020TC006283).
- Park RG, Åhäll KI and Bland MP** (1991) The Sveconorwegian shear-zone network of SW Sweden in relation to mid-Proterozoic plate movements. *Precambrian Research* **49**, 245–60.
- Paterson MS and Wong T-F** (2015) *Experimental Rock Deformation: The Brittle Field*. Berlin, Heidelberg and New York: Springer.
- Pease V, Daly JS, Elming SÅ, Kumpulainen R, Moczydlowska M, Puchkov V, Roberts D, Saintot A and Stephenson R** (2008) Baltica in the Cryogenian, 850–630Ma. *Precambrian Research* **160**, 46–65. doi: [10.1016/j.precamres.2007.04.015](https://doi.org/10.1016/j.precamres.2007.04.015).
- Pevear DR** (1999) Illite and hydrocarbon exploration. *Proceedings of the National Academy of Sciences of the United States of America* **96**, 3440–6. doi: [10.1073/pnas.96.7.3440](https://doi.org/10.1073/pnas.96.7.3440).
- Phillips TB, Jackson CAL, Bell RE and Duffy OB** (2018) Oblique reactivation of lithosphere-scale lineaments controls rift physiography: the upper-crustal expression of the Sorgenfrei–Tornquist Zone, offshore southern Norway. *Solid Earth* **9**, 403–29. doi: [10.5194/se-9-403-2018](https://doi.org/10.5194/se-9-403-2018).
- Pinán-Llamas A, Andersson J, Möller C, Johansson L and Hansen E** (2015) Polyphased foreland-vergent deformation in a deep section of the I Ga Sveconorwegian orogen. *Precambrian Research* **265**, 121–49.
- Quensel P** (1916) Zur Kenntnis der Mylonitbildung, erläutert an Minaral aus dem Kebnekaise gebiet. *Bulletin of the Geological Institution of the University of Uppsala* **15**, 91–117.
- Ramberg IB and Larsen BT** (1978) Tectonomagmatic evolution. In *The Oslo Paleorift: A Review and Guide to Excursions* (eds JA Dons and BT Larsen), pp. 55–73. Trondheim: Norges Geologiske Undersøkelse.
- Redfield TF and Osmundsen PT** (2009) The Tjellefonna fault system of Western Norway: linking late-Caledonian extension, post-Caledonian normal faulting, and Tertiary rock column uplift with the landslide-generated tsunami event of 1756. *Tectonophysics* **474**, 106–23. doi: [10.1016/j.tecto.2009.02.006](https://doi.org/10.1016/j.tecto.2009.02.006).
- Rotevatn A, Kristensen TB, Ksienzyk AK, Wemmer K, Henstra GA, Midtkandal I, Grundvåg S-A and Andresen A** (2018) Structural inheritance and rapid rift-length establishment in a multiphase rift: the East Greenland Rift System and its Caledonian Orogenic ancestry. *Tectonics* **37**, 1858–75. doi: [10.1029/2018TC005018](https://doi.org/10.1029/2018TC005018).
- Rutter EH, Holdsworth RE and Knipe RJ** (2001) The nature and tectonic significance of fault-zone weakening: an introduction. In *The Nature and Tectonic Significance of Fault Zone Weakening* (eds RE Holdsworth, RA Strachan, JF Magloughlin and RJ Knipe), pp. 1–11. Geological Society of London, Special Paper no. 186. doi: [10.1144/GSL.SP.2001.186.01.01](https://doi.org/10.1144/GSL.SP.2001.186.01.01).
- Salomon E, Koehn D and Passchier C** (2015) Brittle reactivation of ductile shear zones in NW Namibia in relation to South Atlantic rifting. **34**, 70–85. doi: [10.1002/2014tc003728](https://doi.org/10.1002/2014tc003728).
- Samsu A, Cruden AR, Molnar NE and Weinberg RF** (2021) Inheritance of penetrative basement anisotropies by extension-oblique faults: insights from analogue experiments. *Tectonics* **40**, e2020TC006596. doi: [10.1029/2020TC006596](https://doi.org/10.1029/2020TC006596).
- Scheiber T and Viola G** (2018) Complex bedrock fracture patterns: a multi-pronged approach to resolve their evolution in space and time. *Tectonics* **37**, 1030–62. doi: [10.1002/2017TC004763](https://doi.org/10.1002/2017TC004763).
- Scheiber T, Viola G, Bingen B, Peters M and Solli A** (2015) Multiple reactivation and strain localization along a Proterozoic orogen-scale deformation zone: the Kongsberg–Telemark boundary in southern Norway revisited. *Precambrian Research* **265**, 78–103. doi: [10.1016/j.precamres.2015.03.009](https://doi.org/10.1016/j.precamres.2015.03.009).
- Scheiber T, Viola G, van der Lelij R, Margreth A and Schönenberger J** (2019) Microstructurally-constrained versus bulk fault gouge K–Ar dating. *Journal of Structural Geology* **127**, 103868. doi: [10.1016/j.jsg.2019.103868](https://doi.org/10.1016/j.jsg.2019.103868).
- Schleicher AM, Sutherland R, Townend J, Toy VG and van der Pluijm BA** (2015) Clay mineral formation and fabric development in the DFDP-1B borehole, central Alpine Fault, New Zealand. *New Zealand Journal of Geology and Geophysics* **58**, 13–21. doi: [10.1080/00288306.2014.979841](https://doi.org/10.1080/00288306.2014.979841).
- Schomberg AC, Wemmer K, Warr LN and Grathoff GH** (2019) K–Ar age determinations on the fine fractions of clay mineral “Crystallinity Index Standards” from the Paleozoic mudrocks of southwest England. *Clay Minerals* **54**, 15–26.
- Schumacher E** (1975) Herstellung von 99,9997% ^{38}Ar für die $^{40}\text{K}/^{40}\text{Ar}$ Geochronologie. *Geochronologia Chimica* **24**, 441–2.
- Selverstone J, Axen GJ and Luther A** (2012) Fault localization controlled by fluid infiltration into mylonites: formation and strength of low-angle normal faults in the midcrustal brittle-plastic transition. *Journal of Geophysical Research: Solid Earth* **117**. doi: [10.1029/2012JB009171](https://doi.org/10.1029/2012JB009171).
- Sherlock SC, Strachan RA and Jones KA** (2009) High spatial resolution $^{40}\text{Ar}/^{39}\text{Ar}$ dating of pseudotachylites: geochronological evidence for multiple phases of faulting within basement gneisses of the Outer Hebrides (UK). *Journal of the Geological Society* **166**, 1049–59. doi: [10.1144/0016-76492008-125](https://doi.org/10.1144/0016-76492008-125).
- Sherlock SC, Watts LM, Holdsworth RE and Roberts D** (2004) Dating fault reactivation by Ar/Ar laserprobe: an alternative view of apparently cogenetic mylonite-pseudotachylite assemblages. *Journal of the Geological Society* **161**, 335–8.
- Sibson RH** (1977) Fault rocks and fault mechanisms. *Journal of the Geological Society* **133**, 191–213. doi: [10.1144/gsjgs.133.3.0191](https://doi.org/10.1144/gsjgs.133.3.0191).
- Sibson RH** (1985) A note on fault reactivation. *Journal of Structural Geology* **7**, 751–4. doi: [10.1016/0191-8141\(85\)90150-6](https://doi.org/10.1016/0191-8141(85)90150-6).
- Sippel J, Saintot A, Heeremans M and Scheck-Wenderoth M** (2010) Paleostress field reconstruction in the Oslo region. *Marine and Petroleum Geology* **27**, 682–708. doi: [10.1016/j.marpetgeo.2009.08.010](https://doi.org/10.1016/j.marpetgeo.2009.08.010).
- Skjerna L** (1972) The discovery of a regional crush belt in the Ørje area, south-east Norway. *Norsk Geologisk Tidsskrift* **52**, 459–61.
- Slagstad T, Roberts NMW, Marker M, Rohr TS and Schiellerup H** (2013) A non-collisional, accretionary Sveconorwegian orogen. *Terra Nova* **25**, 30–37. doi: [10.1111/ter.12001](https://doi.org/10.1111/ter.12001).
- Starmer IC** (1996) Oblique terrane assembly in the late Paleoproterozoic during the Labradorian–Gothian Orogeny in southern Scandinavia. *The Journal of Geology* **104**, 341–50.
- Starmer IC** (1985) The evolution of the South Norwegian Proterozoic as revealed by the major and mega-tectonics of the Kongsberg and Bamble sectors. In *The Deep Proterozoic Crust in the North Atlantic Provinces* (eds AC Tobi and JL Touret), pp. 259–90. Dordrecht: Springer.
- Steiger RH and Jäger E** (1977) Subcommittee on Geochronology: Convention on the Use of Decay Constants in Geo- and Cosmochronology. *Earth and Planetary Science Letters* **36**, 359–62. doi: [10.1016/0012-821X\(77\)90060-7](https://doi.org/10.1016/0012-821X(77)90060-7).
- Stephens MB, Wahlgren C-H, Weijermars R and Cruden AR** (1996) Left-lateral transpressive deformation and its tectonic implications, Sveconorwegian Orogen, Baltic Shield, southwestern Sweden. *Precambrian Research* **79**, 261–79.
- Swenson E** (1990) Cataclastic rocks along the Nesodden Fault, Oslo Region, Norway: a reactivated Precambrian shear zone. *Tectonophysics* **178**, 51–65.
- Tartaglia G, Viola G, van der Lelij R, Scheiber T, Ceccato A and Schönenberger J** (2020) “Brittle structural facies” analysis: a diagnostic method to unravel and date multiple slip events of long-lived faults. *Earth and Planetary Science Letters* **545**, 116420. doi: [10.1016/j.epsl.2020.116420](https://doi.org/10.1016/j.epsl.2020.116420).
- Tessi T, Collettini C, Carpenter BM, Viti C and Marone C** (2012) Frictional strength and healing behavior of phyllosilicate-rich faults. *Journal of Geophysical Research: Solid Earth* **117**, B09402. doi: [10.1029/2012JB009204](https://doi.org/10.1029/2012JB009204).
- Tillberg M, Drake H, Zack T, Kooijman E, Whitehouse MJ and Åström ME** (2020) In situ Rb–Sr dating of slickenfibres in deep crystalline basement faults. *Scientific Reports* **10**, 562. doi: [10.1038/s41598-019-57262-5](https://doi.org/10.1038/s41598-019-57262-5).
- Torgersen E and Viola G** (2014) Structural and temporal evolution of a reactivated brittle-ductile fault – Part I: fault architecture, deformation history and strain localization mechanisms. *Earth and Planetary Science Letters* **407**, 205–20.
- Torgersen E, Viola G, Zwingmann H and Harris C** (2015a) Structural and temporal evolution of a reactivated brittle-ductile fault – Part II: dating fault initiation and reactivations by K–Ar analysis of synkinematic illite. *Earth and Planetary Science Letters* **410**, 212–24.
- Torgersen E, Viola G, Zwingmann H and Henderson IHC** (2015b) Inclined K–Ar illite age spectra in brittle fault gouges: effects of fault reactivation and wall-rock contamination. **27**, 106–13. doi: [10.1111/ter.12136](https://doi.org/10.1111/ter.12136).
- Ulmus J, Möller C, Page L, Johansson L and Ganerød M** (2018) The eastern boundary of Sveconorwegian reworking in the Baltic Shield, defined by $^{40}\text{Ar}/^{39}\text{Ar}$ geochronology across the southernmost Sveconorwegian

- Province. *Precambrian Research* **307**, 201–17. doi: [10.1016/j.precamres.2018.01.008](https://doi.org/10.1016/j.precamres.2018.01.008).
- van der Pluijm BA, Hall CM, Vrolijk PJ, Pevear DR and Covey MC** (2001) The dating of shallow faults in the Earth's crust. *Nature* **412**, 172–5. doi: [10.1038/35084053](https://doi.org/10.1038/35084053).
- Vaucher A, Tommasi A and Barruol G** (1998) Rheological heterogeneity, mechanical anisotropy and deformation of the continental lithosphere. *Tectonophysics* **296**, 61–86. doi: [10.1016/S0040-1951\(98\)00137-1](https://doi.org/10.1016/S0040-1951(98)00137-1).
- Velde B** (1965) Experimental determination of muscovite polymorph stabilities. *American Mineralogist* **50**, 436–49.
- Viola G, Henderson IHC, Bingen B and Hendriks BWH** (2011) The Grenvillian-Sveconorwegian orogeny in Fennoscandia: back-thrusting and extensional shearing along the “Mylonite Zone”. *Precambrian Research* **189**, 368–88. doi: [10.1016/j.precamres.2011.06.005](https://doi.org/10.1016/j.precamres.2011.06.005).
- Viola G, Musumeci G, Mazzarini F, Tavazzani L, Torgersen E, van der Lelij R and Aldega L** (2022) Structural characterization and K-Ar illite dating of reactivated, complex and heterogeneous fault zones: lessons from the Zuccale Fault, Northern Apennines. *EGU sphere* **2022**, 1–35. doi: [10.5194/egusphere-2022-229](https://doi.org/10.5194/egusphere-2022-229).
- Viola G, Scheiber T, Fredin O, Zwingmann H, Margreth A and Knies J** (2016) Deconvoluting complex structural histories archived in brittle fault zones. *Nature Communications* **7**, 13448. doi: [10.1038/ncomms13448](https://doi.org/10.1038/ncomms13448).
- Viola G, Torgersen E, Mazzarini F, Musumeci G, van der Lelij R, Schönenberger J and Garofalo PS** (2018) New constraints on the evolution of the Inner Northern Apennines by K-Ar dating of Late Miocene-Early Pliocene compression on the island of Elba, Italy. **37**, 3229–43. doi: [10.1029/2018tc005182](https://doi.org/10.1029/2018tc005182).
- Viola G, Zwingmann H, Mattila J and Kapyaho A** (2013) K-Ar illite age constraints on the Proterozoic formation and reactivation history of a brittle fault in Fennoscandia. *Terra Nova* **25**, 236–44. doi: [10.1111/Ter.12031](https://doi.org/10.1111/Ter.12031).
- Vissers RLM, Ganerød M, Pennock GM and van Hinsbergen DJJ** (2020) Eocene seismogenic reactivation of a Jurassic ductile shear zone at Cap de Creus, Pyrenees, NE Spain. *Journal of Structural Geology* **134**, 103994. doi: [10.1016/j.jsg.2020.103994](https://doi.org/10.1016/j.jsg.2020.103994).
- Vrolijk P, Pevear D, Covey M and LaRiviere A** (2018) Fault gouge dating: history and evolution. *Clay Minerals* **53**, 305–24. doi: [10.1180/clm.2018.22](https://doi.org/10.1180/clm.2018.22).
- Wahlgren C-H and Kähr A-M** (1977) Mica-lamprophyres in western Värmland, south-western Sweden. *Geologiska Föreningen i Stockholm Förhandlingar* **99**, 291–5.
- Wang Y, Zhou L, Zwingmann H, Lo C-H, Li G and Hao J** (2020) $^{40}\text{Ar}/^{39}\text{Ar}$ dating of cataclastic K-feldspar: a new approach for establishing the chronology of brittle deformation. *Journal of Structural Geology* **131**, 103948. doi: [10.1016/j.jsg.2019.103948](https://doi.org/10.1016/j.jsg.2019.103948).
- Warr LN** (2018) A new collection of clay mineral “Crystallinity” Index standards and revised guidelines for the calibration of Kübler and Árkai indices. *Clay Minerals* **53**, 1–12.
- Warr LN and Rice AHN** (1994) Interlaboratory standardization and calibration of clay mineral crystallinity and crystallite size data. *Journal of Metamorphic Geology* **12**, 141–52.
- Watterson J** (1975) Mechanism for the persistence of tectonic lineaments. *Nature* **253**, 520–2. doi: [10.1038/253520b0](https://doi.org/10.1038/253520b0).
- Wehrens P, Baumberger R, Berger A and Herwegh M** (2017) How is strain localized in a meta-granitoid, mid-crustal basement section? Spatial distribution of deformation in the central Aar massif (Switzerland). *Journal of Structural Geology* **94**, 47–67. doi: [10.1016/j.jsg.2016.11.004](https://doi.org/10.1016/j.jsg.2016.11.004).
- Wemmer K, Steenken A, Müller S, de Luchi MGL and Siegesmund S** (2011) The tectonic significance of K/Ar illite fine-fraction ages from the San Luis Formation (Eastern Sierras Pampeanas, Argentina). **100**, 659–69. doi: [10.1007/s00531-010-0629-8](https://doi.org/10.1007/s00531-010-0629-8).
- Wiest JD, Jacobs J, Fossen H, Ganerød M and Osmundsen PT** (2021) Segmentation of the Caledonian orogenic infrastructure and exhumation of the Western Gneiss Region during transtensional collapse. *Journal of the Geological Society* **178**. doi: [10.1144/jgs2020-199](https://doi.org/10.1144/jgs2020-199).
- Zwingmann H and Mancktelow N** (2004) Timing of Alpine fault gouges. *Earth and Planetary Science Letters* **223**, 415–25. doi: [10.1016/j.epsl.2004.04.041](https://doi.org/10.1016/j.epsl.2004.04.041).
- Zwingmann H, Offler R, Wilson T and Cox SF** (2004) K-Ar dating of fault gouge in the northern Sydney Basin, NSW Australia: implications for the breakup of Gondwana. *Journal of Structural Geology* **26**, 2285–95. doi: [10.1016/j.jsg.2004.03.007](https://doi.org/10.1016/j.jsg.2004.03.007).